UNIVERSITY OF PADOVA

Department of Industrial Engineering

Master degree in Materials Engineering

EFFECT OF LASER POWER AND GEOMETRY ON MICROSTRUCTURAL EVOLUTION OF STAINLESS STEEL IN ADDITIVE MANUFACTURING

Author:

Sebastiano Piazza

Supervisor:

Prof. Manuele Dabalà

Dr. Mert Celikin

The thesis is the result of collaboration with the School of Mechanical and Materials Engineering, University College Dublin in part fulfilment of the requirements for the degree.

Accademic year 2018/2019

ACKNOWLEDGEMENTS

I would like to thank my supervisor Dr. Mert Celikin, without whom this thesis would not has been made, for his guidance through each stage of the process, the invaluable aid during the writing of this work, the pecision in the suggestions, the patience and precious life advices: thank you!

I am grateful to the I-Form Advanced Manufacturing Research Centre for helping and providing the fundings for the project. A special mention goes to Brian J.Merrigan for his unfailing assistance and support throughout the designing and printing phase.

I would also like to thank prof. Manuele Dabalà for encouraging the collaboration between the universities and promptly accepting to be my home institution's supervisor for this work, making it possible.

My deep gratitude goes to my parents for being enthusiasts in each and every little step I made, supportive during this abroad experience and my studies. A special thank goes to my siblings, Federico for always being available providing technical and spiritual assistance, and Beatrice for her tireless optimism and emotional support. Thank you for having supported me along the way and in my life in general.

ABSTRACT

The present work investigates the microstructural evolution of 316L stainless steel samples made through powder bed fusion technology. To do so, the research focused on two different geometries, cylindrical and conical, at three increasing values of laser power: $60\,W$, $65\,W$ and $70\,W$ respectively. All the other processing parameters such as scan velocity, hatch spacing, layer thickness and spot size are kept fixed. A simple analytical model has been used to select suitable laser levels, along with other processing parameters, and to get more insight regarding the resultant melt pool geometry. Microstructural chracterization is carried out at different points of the same specimen, respectively 20%, 50% and 80% of the total height of the part and along its longitudinal axis. A decrease in melt pool depths towards the building direction is determined in all the printed samples, not predicted in the mathematical model. Consequently, a new factor is defined and implemented to better fit the melt pools depth data found. The samples are built with the same base diameter and height to enable univocal correlation, other than to specific laser power value, also to any geometric variation. Furthermore, the increasing complexity exhibited by the two geometries allow the correlation between microstructural evolution and the geometrical factor. Moreover, to further characterize the samples' surfaces Vickers hardness tests are performed. The tests highlighted an increase of hardness with the height of the surface analysed, more consistent in the conical shape compared to the cylinder. The results confirms previous findings about laser power's effect and contributes to validate the used mathematical model, while also contributing to extend the knowledge about geometrical effect on the microstructure.

SOMMARIO

Il presente lavoro indaga l'evoluzione microstrutturale di campioni in acciaio inossidabile 316L realizzati mediante tecnologia di fusione laser a letto di polvere di metallo. Per fare ciò, la ricerca si è concentrata su due diverse geometrie, cilindrica e conica, a tre valori crescenti della potenza del laser, rispettivamente: $60\,W$, $65\,W$ and $70\,W$. Tutti gli altri parametri di processo come la velocità e diametro del fascio laser, spaziatura tra scan consecutive e lo spessore dello strato di polvere sono mantenuti costanti. Un modello analitico è stato utilizzato per selezionare adeguati valori della potenza del laser e degli altri parametri di processo, oltre che per ottenere maggiori informazioni sulla geometria delle pozze di fusione. Caratterizzazione microstrutturale è stata eseguita in diversi punti dello stesso campione, rispettivamente a 20%, 50% e 80% dell'altezza totale della parte e lungo il suo asse longitudinale. In tutti i campioni stampati si è osservata una diminuzione della profondità delle pozze di fusione lungo la direzione di stampaggio, non prevista nel modello matematico. Di conseguenza, è stato definito ed implementato nel modello un nuovo fattore in grado di descrivere meglio i dati di profondità trovati. I campioni presentano uguali diametro di base e altezza per consentire una correlazione univoca, oltre che dalla potenza del laser, anche per qualsiasi variazione geometrica. Inoltre, la crescente complessità mostrata dalle due geometrie consente buona correlazione tra l'eventuale evoluzione microstrutturale ed il fattore geometrico. In aggiunta, per caratterizzare ulteriormente le superfici dei campioni, sono stati eseguiti test di durezza Vickers. I test hanno evidenziato un aumento della durezza con l'altezza della superficie analizzata, più coerente nella forma conica rispetto a quella cilindrica. I risultati confermano precedenti lavori sull'effetto della potenza del laser e contribuiscono a convalidare il modello matematico utilizzato, contribuendo anche ad estendere le conoscenze sull'effetto della geometria sulla microstruttura.

CONTENTS

LIST OF FIGURES

LIST OF TABLES

INTRODUCTION

In the last decade the interest in additive manufacturing techniques is grown exponentially, especially in those sector where high added value components are produced such as aerospace or biomedical. Primarily because it enables flexible production of highly customized products by avoiding any cost penalties related to manufacturing and reducing material's waste.

3D printing techniques has already been applied to a wide range of materials, recently the most researched are steels, titanium alloys and aluminium alloys. However, metals need particular processing condition to be printed and their resultant structure differ from traditionally casted microstructure; thus, arising difficulties when predicting the components' quality. In this perspective, it is important to have control over the printing process to enable desired properties to be achieved through proper microstructure tuning. In the literature, many studies focus on correlating either the processing parameters with the resultant microstructure or with mechanichal properties. It is known that laser power is the main factor in influencing the heat source and, consequently, the thermal gradient (G) and the liquid-solid interface velocity (R) which can be related to possible variations in the resulting microstructure. While, section's variation in the geometry affects its heat capacity extraction during printing, thus leading to possible structure features changes and defects. Therefore, the aim of this thesis is to investigate the effect of geometry, a parameter not often taken in consideration in the literature due to difficulties in obtaining univocal results; a problem that has been addressed in the present work. Furthermore, this work also wish to investigate the effect of laser power, to validate the mathematical model used to predict the process outcomes in terms of melt pools geometry, meanwhile endorsing what is already being made in the literature. Eventually, it aspires

to propose an improvement in the mathematical model to better predict the resulting melt pools geometry from the process parameters.

This thesis is composed of four Parts: Overview of additive manufacturing, in which is summarized the literature supporting this work; Materials and methods, containing a brief description of the experiments and the instruments utilized; Results and discussion, in which all the data obtained from the experiments is presented and analysed; Conclusions, containing an overview of the final assessment. Each part contain three chapters, exception made for the fourth part, for a total of ten chapters subsequently divided in sections and subsections.

In the first chapter an introduction to additive manufacturing is given, with particular focus on laser powder-bed fusion technique used in this work. While, chapter two summarize the different types of stainless steel from a metallurgical point of view, empathising the steel grade used in the printings. The third chapter use the information contained in previous sections to address the major parameters that can affect the printing process with in-depth details from other literature studies.

Then, the reasoning behind the selected geometries and processing parameters is explained in the fourth chapter, while summarizing the settings used during the printing. Chapter five gives a detailed overview of the instruments used throughout the thesis, while in chapter six the characterization methods are presented.

Moving on, in chapter seven the findings from the microstructural analysis are properly divided to highlight laser power and geometry effects on the structure. Moreover, the melt pools data, divided by depth, width and length, are reported and properly discussed with particular focus on the trend found in the melt pools depth validated with statistical analysis of variance. Chapter eight present the results obtained from Vickers hardness tests divided in a similar fashion to the previous chapter. Then, in chapter nine further analysis on the melt pools depth data is done to gain insight from the trend interpolation; this lead to the definition of a new factor used

as an input into the predicting mathematical model to better describe the trend found in chapter seven.

Lastly, chapter ten gives a brief summary of the findings from all the experiments done and proposes possibles future studies originated from the present work.

Part I

OVERVIEW OF ADDITIVE MANUFACTURING

1 ADDITIVE MANUFACTURING

Additive manufacturing (AM) is a process where materials are applied in successive layers to make three-dimensional solid objects of virtually any shape from a digital model. It is an additive process clearly distinguished from traditional subtractive machining since they rely on material removal by methods of cutting, milling, grinding, etc. Further, AM presents a wide range of different technology that share the common principle of building parts layer by layer while differs in the feedstock type used, mainly powder, wire or liquid solution, and the mechanism of layer consolidation, through a heat source such as laser or electron beam, or light in the case of a photopolymer resin. In addition to that, this technology offers various advantages, among all the most important ones are unmatched design freedom and relatively short production times compared to traditional methods.

In recent years, thanks to the development of printing machines able to work with metals, interest in AM has rose. Thus, the possibility to obtain complex shapes combined with the advantages above said, lead to many different research studies with expensive metal alloys commonly used in fields like biomedical and aerospace, in which relatively low number of parts with high complexity is required.

In the 1980' rapid prototyping was first developed to help, in a quick and affordable way, the realization of complex parts in order to cut down the product development process [1, 72]. According to the ISO/ASTM 52900, AM is defined as: *"The process of joining materials to make objects from 3D model data, usually layer upon layer, as opposed to subtractive manufacturing technologies"* [61]. Subtractive manufacturing is the retronym who address conventional machining process, such as turning, milling or grinding in which the products are fabricated from a stock by material removal [25]. In AM,

through successively adding material layer by layer avoid the constraints caused by tooling and enables the possibility of any shape to be created. Thus, efficient usage of raw materials is achieved with satisfactory geometric accuracy [39]. AM is the perfect example of a flexible manufacturing technology, since it can theoretically achieve a wide variety of outcomes in manufacturing with the usage of one machine paired with the ability of produce 'on demand' [11, 52]. Setup and changeover costs are negligible, only a computer-aided design (CAD) model is needed, compared to a traditional manufacturing process in which tools and molds are necessary [50]. Thus, product individualization and functionally optimized product designs is achieved without additional costs. Besides time and cost savings, AM present several other advantages such as material efficiency, since leftover materials can be reused with minimum processing; reduction of errors form incorrect interpretation of the design prototype and related iterations are faster; depending on the technology, models produced can be used as patterns for casting; if required and, with appropriate materials are usage, AM can serves in assembling operation where different fabricated parts can be combined to create the final component [51]. Still, the main advantage of AM technology is by far flexible production of highly customized products by avoiding any cost penalties related to manufacturing. Further, several functions such as moving parts or cooling systems can be integrated while processing the component without the addition of assembly or manufacturing steps [49]. Therefore, AM technology affects the costs of flexibility and individualization, marginal production costs and capital costs [10, 39]. Although, it must be said that AM present a number of limitations that need to be addressed. Material's characteristics differs from conventional manufacturing processes and usually an additional surface finish operation is requested. Moreover, the lower production speed creates the needs to balance a fairly complex part with a minimal production rate, in order to have a higher cost effectiveness compared to traditional manufacturing [3]. Just in 2011, AM market generated $1.714 billion in revenue, which includes $834 million for additive manufacturing systems and materials; $642.6 million

from the sale of parts produced; and $236.9 million for maintenance contracts, training, advertising, and consulting [64]. A glimpse on the recent growth of this technology can be seen by the forecast of the future market. In 2011 the industry was estimated to reach $50 billion between 2029 and 2031, while reaching $100 billion between 2031 and 2044 [65]. Whereas, in a more recent study forecasted that by 2025 AM will have an economic impact of $200 to $600 billions annually [41]

AM definition can be applied to all classes of materials including metals, ceramics, polymers, composites and biological systems. AM feedstock are typically divided in to three categories: powder, wire or sheets. They influence the AM process in which the feed stock is consolidate into a dense 3D object. Consolidation can be achieved either by melting or solid state joining during the process [23]. There are many distinct class of AM processes which usually differs from the type of raw material input and the energy source used to form the part. From the seven categories listed in the F42 standard, the following four pertain to metal AM:

1. powder bed fusion (PBF);
2. direct energy deposition (DED);
3. binder jetting;
4. sheet lamination.

Considering the scope of this work an overall introduction on metal AM technologies will be given, followed by a more detailed focus on the technology used for this research.

DED is being referred to processes where focused energy generates a melt pool into which the feedstock is deposited. The energy source can be laser, arc or electron beam; while the raw material input can be powder or wire. In the process a monolayer of materials is melted into the desired pattern and, through the repetition of this step a 3D component is built. Powder hoppers are filled and a build substrate is positioned either in a stationary position or in a rotating stage in order to enables more complex geometries. Moreover,

two types of working principles can be found: the part remains stationary to the table while the deposition head moves for each layer; the head remains stationary and the work piece is moved. A chamber can enclose the system providing laser safety and a controlled atmosphere to avoid oxidation of the molten weld pool. Some systems deploying a shield gas supply direct to the weld pool can avoid the usage of the chamber. These techniques are well suited for large parts or when repair of damaged part is needed [71]. However, powder-based approach shows a better dimensional accuracy and lower deposition rate; while, wire-based approach present higher deposition rate but lower dimensional control over part's geometries, thus machining of the fabricated parts is typically required.

Binder jetting is essentially a powder metallurgy process. It relies on the usage of a binder deposited on the metal powder which, after curing, will hold the metal powder together. Thus, consolidation of the powder is achieved, typically followed by infiltration with a second metal since the fabricated parts present low density. While designing, shrinkage of the part occurs and the resultant distortion needs to be taken in to account. When the binder dries, the green body, consisting of a fragile binder-metal mix, can be removed from the system; then, it will need to be cured, which can take 6 h to 12 h, and finally heat treated at ~ 1100 °C for 24 h to 36 h to sinter the loose powder and burn off the binder, typically leaving a 60 % dense sintered metal part [57].

Sheet lamination consists of stacking precision cut 2D metal sheets from a 3D object. After stacking, these sheets will be adhesively or metallurgically bonded together using one of several methods like diffusion bonding, laser welding, brazing or ultrasonic consolidation. Sheets can be either cut with the specified geometry prior to adhesion or machined post-adhesion. Some advantages of this process are low geometric distortion and a good surface finish with relatively low cost. On the other hand, shear and tensile loading conditions are critical for the fabricated parts and swelling may occur, thus lowering the geometric accuracy. Sheet lamination is a promising technology

with particular regard for making metal composites by alternating sheets of different metal during consolidation [14].

1.1 POWDER BED FUSION

In powder bed fusion systems the energy source, typically electron beam or laser beam, guided by the digital model, is used to selectively melt or sinter the metal powder with a precise pattern, building up a single layer of material. A general illustration of selective laser melting (SLM) is given in fig. 1.1. The powder delivery system makes use of a piston to supply powder, a coater to create the powder layer, while another piston holds the fabricated part. The reservoir of metal powder is then lowered by a single layer thickness and by raking new powder on top of the part the process can be repeated until the final 3D component is finished. The adherence of each layer is allowed by the re-melt of previous deposited layers during the process. All the systems are enveloped in a chamber that can operate in vacuum or filled with inert gas in order to prevent oxidation of the metal powders. Moreover, the chamber is pre-heated depending on the type of energy source, 100 °C for laser based systems and 700 °C for electron beam technologies [13]. SLM present a system of lenses and a scanning mirror or galvanometer that direction the beam through the desired pattern. Whereas, in electron beam melting (EBM) a high-powered scanning electron microscope (SEM) is used, combined with an electron beam column, and filament magnetic coils to collimate and deflect the beam. Moreover, in order to distribute the powder EBM systems require a powder hoppers and a metal rake while SLM systems typically use a feeding system or powder hoppers and a soft distribution 'recoater' blades which are able to drag the metal powder across the build surface.

Both systems require the following steps: machine set-up, operation, powder recovery and substrate removal. It is important to give mechanical and thermal support to the build material; in PBF machines this is typically

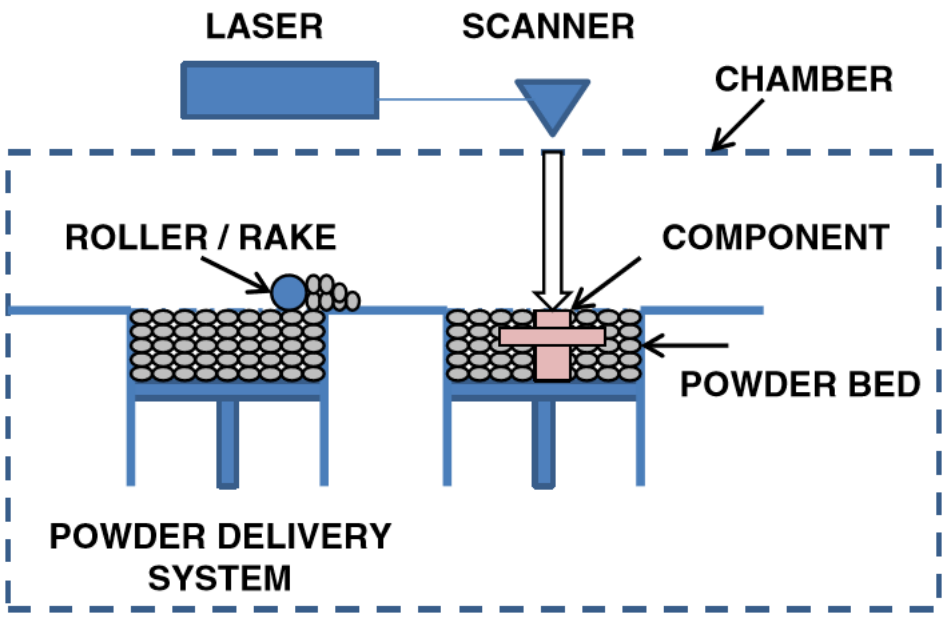

Figure 1.1. Schematic illustration of SLM system [13]

achieved with a built substrate or start plate. For example, in EBM systems the powder that surround the plate prevent the displacement of the plate with the rake blade; whereas, SLM technologies typically clamp down the substrate in order to provide more stability. In the process of adding and rolling out new layers of metal powder, the substrate usually helps provide mechanical support. Moreover, it provides a thermal path to dissipate heat, which is important in certain geometries prone to process defects caused by temperature fluctuations like swelling [57]. After the component is complete, the chamber needs to be cleaned by the excess powders. For EBM parts, the excess powder needs to pass through a recovery system in order to be recover sintered powder and successfully remove it from the surrounding of the component. On the other hand, for SLM processes, the powder around the build usually does not sinter as much and can directly be removed and sifted ready to be re-utilized. Some problems arise when the build substrate adhere to the 3D object. Since the substrate must be cut off, common methods are abrasive saws or wire EDM. Particular material combination of substrate-component can be deployed to promote poor adherence; thus, the build part can be easily removed by an applied force. PBF technologies process pre-alloyed materials, achieving high densities when the process pa-

rameters have been set-up correctly. The main advantages of this system are the ability to produce high resolution features, internal passages while maintaining dimensional control over the part's geometries.

Any material can be used in the PBF as long as it can be produced in atomized form. In the current state of industry, there are several metals and alloys being used: iron based alloys with a particular focus on 17-4, 15-5 and 316L stainless steel, titanium alloys and especially Ti6Al4V, aluminium alloys frequently AlSi10Mg, Cu alloy, Inconel and also composites such as TiAl [58]. Even if it has been shown that AM fabricated parts are weaker than forged and milled parts, they do not present welds which are often cause of failure in many applications [16]. Therefore, AM has been applied across in many industries and potential applications are still increasing with notable sectors being biomedical, aerospace and automotive [33, 59]. As already mentioned, the flexible design and possibility of complex geometries combined with availability of high performance materials enables the usage of AM for metal parts in satellites, helicopters and jet engines [26]. Wide opportunities exist in the biomedical field for the fabrication of custom-shaped orthopaedic prostheses and implants due to the ability to efficiently create porous surface structures that facilitate osseointegration, customized inserts for hip and knee replacements, medical devices, micro-vasculature networks, and heart valve [20, 29, 30, 51].

2 STAINLESS STEEL

In metallurgy, stainless steel (SS), also known as inox, is an iron-based alloy with a minimum content of chromium of 10.5 % and maximum carbon content of 1.2 %. Other elements with the most notable being Ni, Mo and Mn can be always found in any SS alloy since they give a wide range of desired properties. The most notable property of SS is the high corrosion resistance, mainly given by Cr but also enhanced by Mo. The resistance to corrosion derives from the ability of these steels to passivate in oxidizing conditions. The oxygen adsorbed on the surface creates a thin surface film mostly made of chromium oxides such as Cr_2O_3 and $Cr(OH)_3$ that protects the underlying material from further oxidation. Moreover, the oxide film is insoluble, compact, well adherent to the substrate and, if scratched, is reformed in the presence of oxygen, restoring the conditions of corrosion resistance of the steel. The classification of stainless steel is made of five categories and is based upon the nature of their crystalline structure, which is related to the chemical composition of the steel. An overview of the different metallurgical phases can also be observed in the Schaeffler-Delong diagram as fig. 2.1 shows; where the axis are written in terms of nickel and chromium equivalents, with their formulations also expressed in the graph.

(i) austenitic stainless steel;

(ii) ferritic stainless steel;

(iii) martensitic stainless steel;

(iv) duplex stainless steel;

(v) precipitation hardening stainless steel.

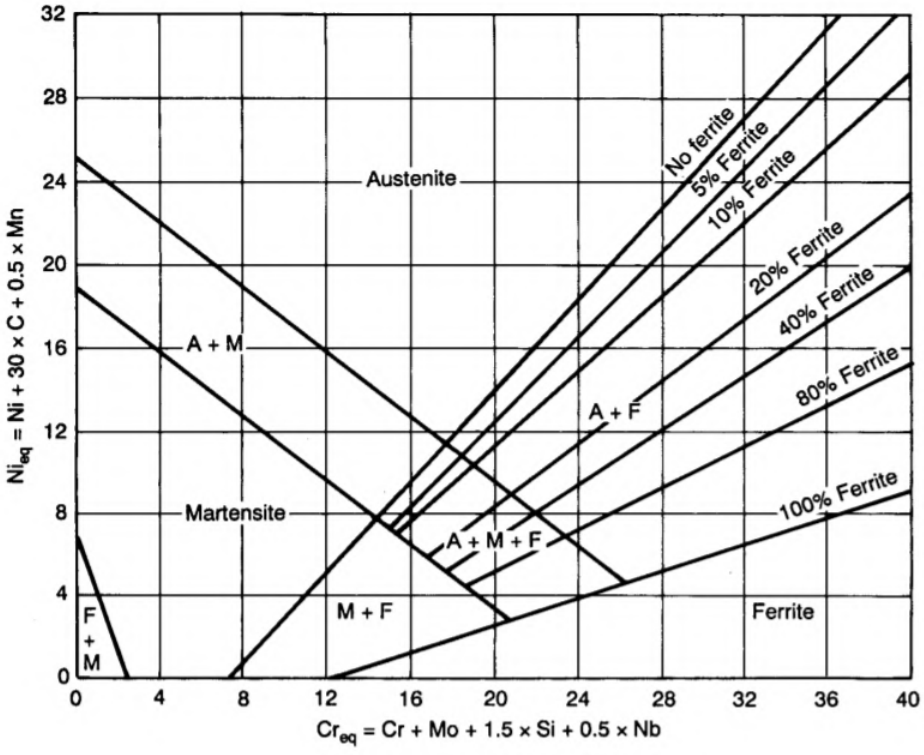

Figure 2.1. Schaeffler-Delong stainless steels constitution diagram [43].

For better clearance, all the above mentioned stainless steel categories will be presented; while a more detailed focus will be given on austenitic stainless steels, topic of this project (see section 2.1).

Ferritic stainless steel exhibit ferrite as a stable phase, which is a body-centered cubic crystal structure. They contain between 10.5÷30% of chromium, carbon content below 0.1 % and very little to no nickel. Similar to austenitic stainless steels ferritic phase is maintained until melting, making this type of steels not hardenable by heat treatment. The microstructure of these steels contains only ferrite grains and an example can be seen below in fig. 2.2. They possess good formability, although present some problems in welding due to excessive grain growth in the heat affected zone. In fact, welding of ferritic stainless steels is made only in thin thicknesses, thus not used in large construction like heavy walled vessels or tanks. These alloys present various forms of embrittlement, they can't be used at lower temperature due to the fragile-ductile transition of the bcc phase at room temperature. It is important to avoid the formation of sigma phase, especially with Cr content above 20 % since it can severely reduce ductility and toughness. They are

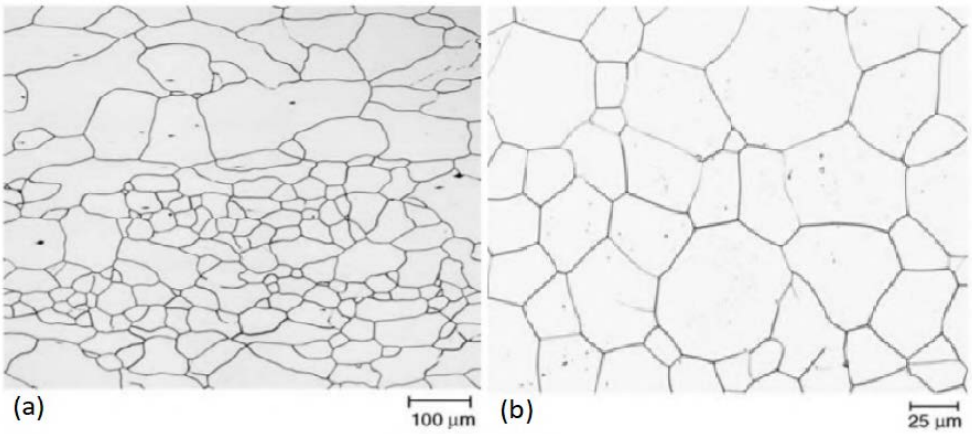

Figure 2.2. Microstructure of 26Cr-1Mo E-Brite ferritic stainless steel at different magnification [67].

susceptible to embrittlement when heated from 400 °C to 540 °C due to the formation of chromium-rich and iron-rich ferrites. In addition to that, high-temperature embrittlement can occur in steels with moderate carbon content when heated above 950°C and cooled to room temperature, which will also result in loos of corrosion resistance. This is caused by the chromium depletion that occur in adjacent areas of precipitated carbides. Usually the last two types of embrittlement can be avoided by applying particular care during the heat treatment and by heating up the steel to a controlled range temperature, approximately between 550 °C to 950 °C, in which neither of the above said phenomenon can occur.

Martensitic stainless steels contain between 10.5÷18% of chromium, nickel content up to 10 % and also relatively high carbon content, usually below 1.2 %. The composition need to be carefully balanced to avoid the formation of δ-ferrite at the austenitizing temperature if best mechanical properties want to be attained. Moreover, the alloying elements main function is to enable the formation of martensite as a metallurgic phase, and by fact, these steels are rapidly quenched from high temperature. The presence of carbon, even if is necessary to achieve good hardness and mechanical resistance of the steel, tents to create chromium carbides which lower corrosion resistance by reducing the Cr content in the surrounding areas. The resulting martesite vary with carbon content: with an increasing content of carbon, martensite would change from lath to plate morphology, becoming finer. These steels

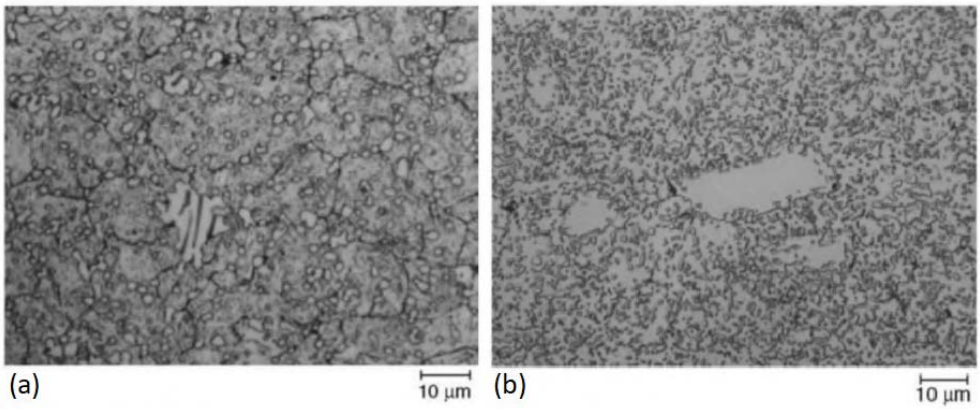

Figure 2.3. Metallography of 440C martensitic stainless steel: (a) after tempering and (b) annealing [67].

can be heat treated, thus providing a wide range of mechanical properties compared to other types of stainless steel even if their corrosion resistance is moderate. Particular attention should be exerted to control the carbide size and distribution, with a uniform dispersion of fine carbides in a ferrite matrix being the desired result. When tempering is taken out, coarser carbides with varied morphology can be seen as in fig. 2.3(a). While, annealing heat treatment result in finer spherical carbides, even if it can be seen the presence of large primary carbides which needs to be addressed.

the text above has been modified!! Have a look at it!!

Duplex stainless steels typical microstructure consists of austenite and ferrite, typically with a ratio of 50/50 or 40/60. They contain between 18÷32% chromium, up to 9 % of nickel, while carbon content tends to be below 0.03 %. Their mixed microstructure provides good strength, toughness and corrosion resistance. The desired microstructure consists of a very fine-grained microduplex structures as it can be seen in fig. 2.4. While in fig. 2.4(a) phase boundaries are well defined, in fig. 2.4(b) electrolytic 20 % NaOH gives a gray colour to ferrite making it easy to recognise. These steels are weldable, although some caution must be exercised to maintain the correct balance of the different phases. All these properties are achieved with an overall lower alloy content than similar performing austenitic grades, which make their use cost-effective in various applications, mainly where the risk of corrosion

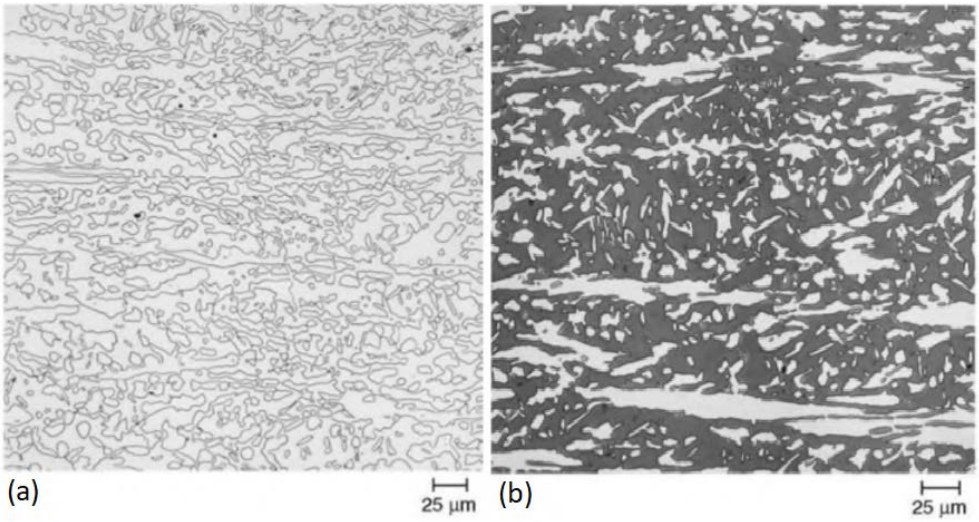

Figure 2.4. Microstructure of 7-Mo PLUS duplex stainless steel etched with: (a) chemical solution of ethanol 15 % HCl; (b) electrolytic solution of aqueous 20 % NaOH at 4 V dc for 10 s [67].

under tension does not allow the use of autenitic stainless steels and where generalized corrosion does not allow the use of ferritics.

Precipitation hardening stainless steels are born with the aim of maintaining the mechanical behaviour of martensitic stainless steels while increasing the resistance to corrosion. They usually contain alloy elements such as aluminium, copper, titanium and, occasionally, molybdenum and niobium to produce the precipitates. Precipitation hardenable grades can be further divided into three categories: martensitic, semi-austenitic and austenitic. These steels usually undergo a solubilisation treatment which make them machinable. All this grades are hardened by a final aging treatment performed in a temperature range between 455 °C to 790 °C, depending on the type of steel, that enables the formation of very fine second-phase precipitates from a supersaturated solid solution. Precipitated particles introduce strains into the lattice, thus achieving the strengthening exhibited by these steels. Among these steels, the most utilized are the martensitic since enhance the mechanical properties even more. The desired microstructure can be seen in fig. 2.5 and consists of tempered martensite with very fine precipiates.

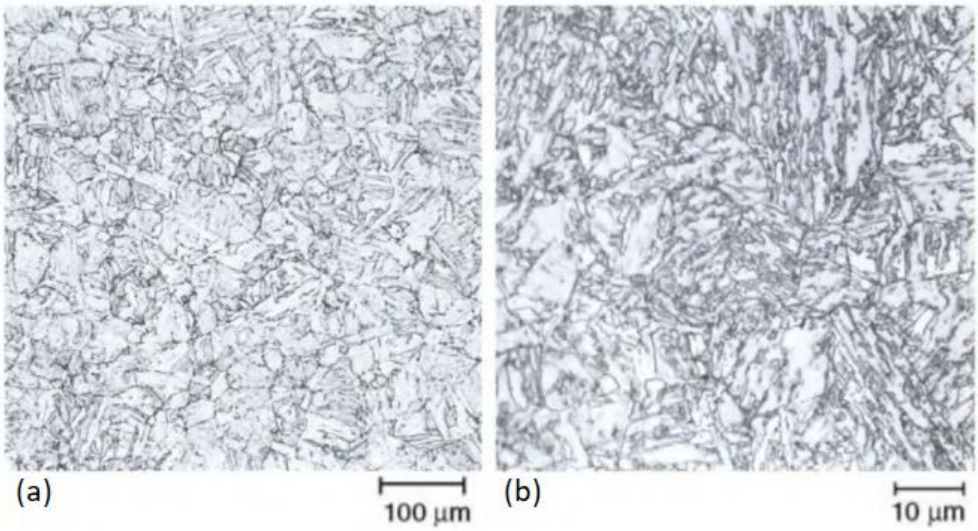

Figure 2.5. Metallography of precipitation hardenable stainless steel: (a)17-4PH; (b)PH13-8Mo [8].

2.1 AUSTENITIC STAINLESS STEEL

Austenitic stainless steel is the largest family since it makes about 60 % of the total steel production. They are made up of austenite, a stable phase consisting on a face-centered cubic crystal structure. The microstructure is achieved by alloying with a percentage of chromium between 16÷26%, and nickel around 6÷22% and sufficient amount of molybdenum that can reach up to 6 % in certain steel. The carbon content is typically lower than 0.1 % and, in low carbon versions like 304L and 316L it is maintained below 0.03 % to prevent precipitation of $M_{23}C_6$ carbides, where M refers to Cr, Fe or Mo, which occur when heated in the range 500 °C to 600 °C and lead to intergranular corrosion, this phenomenon is referred as sensitization. The low carbon content of this grades also cause a greater tendency to delta-ferrite stabilization, which would result in embrittlement. Other additional element that can be added are titanium or copper, to further improve their properties making them suitable for applications in high temperature environment where corrosion resistance is needed. The presence of Ni stabilizes the austenite phase at all temperature making it suitable for cryogenic applications by avoiding the problems related to brittleness, typical to other type of steel. Thus, they cannot be hardened by heat treatment since they present

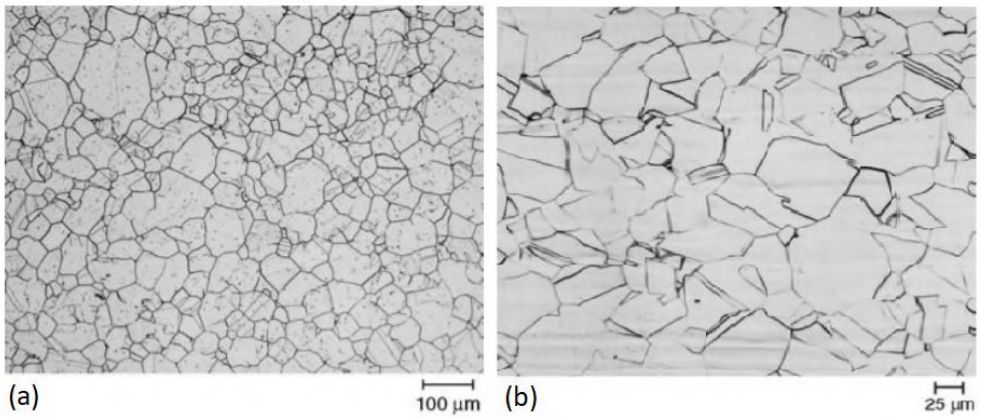

Figure 2.6. Austenitic stainless steel microstructure of (a) 304 SS solution-annealed at 1038 °C for 1 h; (b) 316L SS solution-annealed at 954 °C for 1 h [67].

the same microstructure until melting. An annealing heat treatment, generally at temperature between 1010 °C to 1065 °C, is done with the purpose of retain the carbon in solution, producing a carbide-free austenitic microstructure. The resultant solution-annealed structure should consist of equiaxed grains containing annealing twins, as can be seen in fig. 2.6. Austenitic stainless steel shows high corrosion resistance compared to ferritic and martensitic stainless steel. Although, corrosion performance can be varied to suit different service application environments by varying the C or Mo content. They do not exhibit a yield point and are strengthened by work-hardening. In addition to that, these steels show a greater thermal expansion and heat capacity, with lower thermal conductivity than other stainless steels. Further, the property of being non-magnetic, along with all the other properties listed above, make austenitic stainless steels highly demanded in the biomedical field; where reliable devices needs to be implanted in to the human body for long period of times.

3 ADDITIVE MANUFACTURING OF STAINLESS STEEL 316L

Considered all the advantages above said, AM is a promising technology especially in the biomedical field where complex geometries and customisation is needed. In addition to that, the environment the body creates is particularly severe from the corrosion point of view, and materials need to be carefully design to be able to sustain those in work conditions. Therefore, in body implants applications such as lumbar vertebra, where good corrosion resistance and mechanical properties need to be exerted, austenitic stainless steel grades such as 316L seem to be the optimal solution and have received increasing interest interests within the AM area [9]. Furthermore, given biocompatibility as one of the main concern in the biomedical field, stainless steel was identified as biologically compatible to the human body for long-term applications, with few other metals [21].

Microstructure tuning is necessary if desired mechanical properties want to be achieved in the fabricated part. In fact, the rapid solidification that occur in the process combined with many re-heating and re-cooling cycles that the material undergoes generate hierarchical microstructures. Low magnification levels of a cross-sectional view enable the melted tracks to be seen, as observable below. fig. 3.1 present segregated melt pools with distinct boundaries at two different build direction, with no particular change observable except from a slightly wider melt pool in fig.8b. The powder particles are completely fused together as the melted and solidified zone present curved edges. It is important to note that this result can be seenin both fig. 3.1 and fig. 3.2 and is achieved by overlapping the laser tracks so that every track is able to bond onto the other surrounding tracks. Arrows in fig. 3.2(b) point out defects at the intersection of multiple scan tracks.

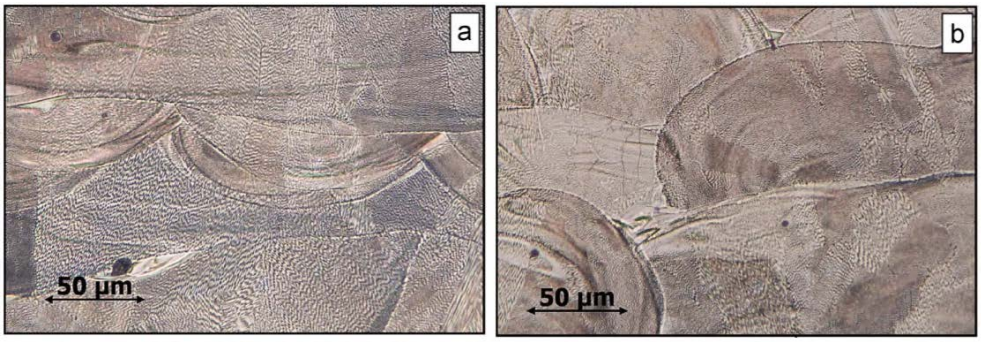

Figure 3.1. 316L stainless steel fabricated at 195 W and 750 mm/s with a horizontal built direction (a) and 45 degree inclined built direction (b) [48].

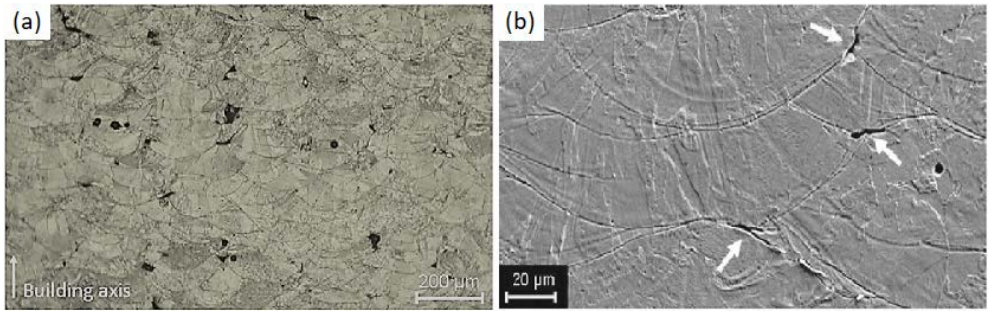

Figure 3.2. Cross-section view of 316L stainless steel fabricated at 105 W and 380 mm/s [74].

AM processes often lead to meta-stable microstructure with resulting phases of non-equilibrium compositions which can vary from layer to layer [24]. In PBF of 316L, ultrafine grains in the order of few microns can be obtained (see fig.10), much smaller than casting where the dendrite cells are in the order of tens of microns, thus leading to superior tensile strength of fabricated materials compared with more traditional methods [75].

The process involves almost 130 parameters that could affect the quality of the final product, in terms of density, residual stress, surface roughness and resulting microstructure. Melt pool formation in PBF is similar to the welding process, when laser or electron beam are used as energy source. The main difference consists on the physics related to the interaction of the energy source with the metal powder, in which radiation absorption, scattering, powder melting and melt wetting have to be considered [33]. Spatter ejection, i.e. the convective transport of liquid or vapour out of the melt pool, needs to be addressed since can be the cause of process-induced porosity. Accurate control of the melt pool length, width and depth is desirable

since it can affect the solidification kinetics (see section 3.1). However, melt pool geometry as well as thermal gradient are also influenced to some extent by the part geometry, since a difference in size would result in different peak temperatures during melting, given heat source power and speed constant [57]. Moreover, local preheating of the material caused by insufficient cooling between hatches or layer can lead to increasing melt pool dimension which then would lead to poor control of the process [27].

Although many parameters can be found that affect the process in different ways, some of them influence more aspects of the process than the others. Therefore, it is possible to identify the factors that have a major influence: laser power P (W), scan speed v (mm/s), hatch spacing h (mm) and powder layer thickness t (mm); these parameters have the highest impact in to the resulting material properties and can be combined by defining the volumetric energy density E (J/mm^3) as shown in eq. (3.1) [17]. The volumetric energy density is a thermodynamic term that quanties the amount of energy reaching the powder bed [75].

$$E = \frac{P}{v \cdot h \cdot t} \tag{3.1}$$

Some studies found a critical value of energy density, in which material undergoes unstable melting when exposed to values above this critical point leading to vaporisation and microsegregation phenomenon. Moreover, using lower energy density than the critical level would still cause void formation due to gas pores or discontinuous melt tracks [73]. However, it seems that the critical energy density varies depending on the machine used (see section 4.3). Further, other research reported that the volumetric energy density may not be a good indicator for porosity in the fabricated parts [17]. Therefore, a good practice when approaching laser powder bed fusion (L-PBF) would be to look at the volumetric energy density as a general indicator of the process, while still focusing more attention on selecting the optimal parameters, which in turn seems to play a bigger role in influencing the printing. A brief description of important factors that can influence the quality of the

fabricated part will be given later on (see from section 3.2 to section section 3.5). Although, it is important to mention that will not be an exhaustive description since it is not the aim of this work.

3.1 HEAT TRANSFER

Generally speaking, transfer of heat in AM can occur through conduction to the substrate, conduction to the build material and convection to the shield gas. Although, in PBF the thermal insulating effect of the metal powder surrounding the part also need to be considered. The mode of heat transfer has several remarkable microscopic implications. For example, the depth of the melt pool is a dynamic equilibrium controlled by the conduction of heat between the melt pool itself and the material underneath [34]. The melt pool is influenced by the heat source power (see section 3.2), speed and size and also relate to the solidification which determines the phase distribution and grain morphology of the deposited layer. In addition to that the thermal cycling can enable further precipitation, phase growth and grain growth. Depending on which path the heat source take while building a layer, the heat from previous pass may not have time to dissipate. In this particular aspect, the poor thermal conductivity of the metal powder plays a big role [70]. Moreover, in order to achieve a fully dense fabricated part good adhesion between layers is mandatory; thus, to ensure a good adhesion the heat source need to penetrate several metal layers. Therefore, some layers will be remelted, usually leading to a non-equilibrium microstructure with high internal stresses [37]. The beam power and speed also affect the thermal gradient (G) and the liquid-solid interface velocity (R) of the melt pool. These factors are used to calculate the columnar-to-equiaxed transition (CET) and to predict the resultant grain structure as described by the undercooling criterion. The G over R ratio from high to low value determines consecutively a planar, columnar and equiaxed dendritic structure. While

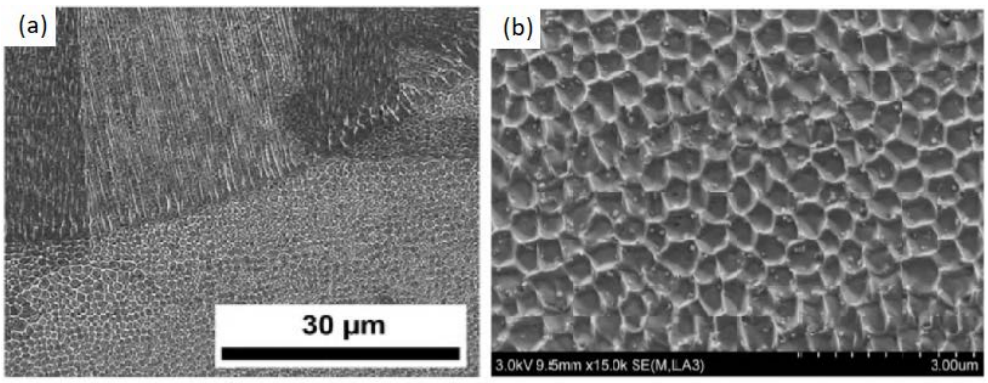

Figure 3.3. Microstructures of 316L stainless steel fabricated at (a) 60 W and 30 mm/s [4]; (b) 300 W and 800 mm/s [68].

the cooling rate (i.e. GxR) controls the fineness of the structure, thus higher product lead to finer grains [27].

Although, variations of the temperature gradient and thermal flux can result in a mixed microstructure. Typical microstructures obtained in PBF consists of columnar grains highly oriented in the build direction i.e. the heat flux, or ultra-fine cellular dendrites. In fig. 3.3, distinct microstructures in neighbour solidified melt pool. More orientated grains are present in the upper melt pool of fig. 3.3a; while a fine cellular structure is visible at the bottom and the pattern is clearly shown in fig. 3.3b with higher magnification.

3.2 LASER POWER

The importance of this parameter for the whole process is remarkable since it's the controlling factor of the heat source. Thus, it has huge impact in the melt pool formation and in the thermal gradient evolution, which then affect void formation, resulting microstructure, residual stresses, delamination and swelling. Although, it needs to be kept in mind that laser power and scan velocity are paired parameters and different combination of the two can produce similar effects. In PBF, what need to be addressed is the beam-powder interaction. In fact, depending on the laser power, the mechanism for melting the powder and the molten material behaviour will

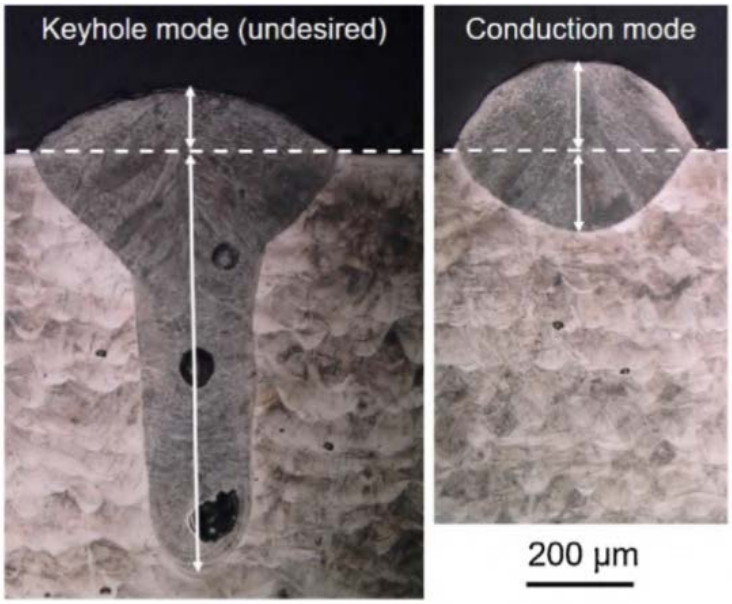

Figure 3.4. Selective Laser Melting of stainless steel 316L, melt pool morphology typical of keyhole mode melting (left) and conduction mode melting (right) [46].

change from being controlled by thermal conduction to being controlled by the keyhole-mode melting. In the keyhole-mode laser melting, high power of the beam causes the evaporation of the metal and the formation of plasma. This enable the beam to form a cavity and reach deeper depth; collapse of the cavity can entrap gasses with the following formation of voids, resulting in poor quality of the build part [31]. Furthermore, voids formation can also be caused by powder denudation effects, mainly related to the entrainment of particles by surrounding gas flow. The flow is induced by the intense evaporation that occurs in the laser spot and the resultant pressure drop associated to the Bernoulli effect [42]. fig. 3.4 well illustrate the above said paragraph with two examples of the melting mechanism that can occur in AM.

It is important to say that pores in AM of metals is a common defect that need to be addressed since it negatively affect mechanical properties. Process parameters, especially laser power, need to be properly tuned to minimise pores formation. There are several types of porosity: powder-induced, process-induced or an artefact of solidication. During powder atomisation, gas pores can be entrapped inside the powder feedstock and directly trans-

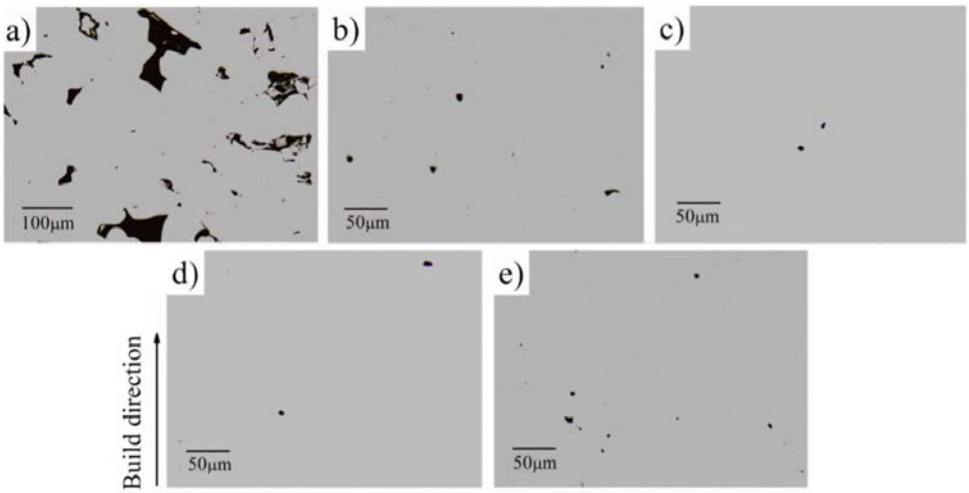

Figure 3.5. Optical micrographs (a)-(e) of 0.5 P_0, 0.7 P_0, P_0, 1.3 P_0 and 1.5 P_0 respectively, where P_0 refer to the optimized setting [75].

late in to the printed part. Process-induced porosity is usually caused by either lack of fusion or spatter ejection phenomena. Shrinkage porosity refer to the incomplete flow of melted metal in a certain region [57]. Obviously, while shrinkage and powder-induced porosity present higher correlation respectively with the feedstock composition and atomisation process, laser power relate to process-induced porosity. Therefore, lower laser power usually results in large irregular voids related to lack of fusion; whereas, high laser power typically shows spatter ejection defects and thermally-induced cracks due to temperature gradient and residual stress. These situations are illustrated in fig. 3.5 at increasing levels of power laser, where black regions represent pores or cracks; best quality of the fabricated part (i.e. high density and good fatigue resistance) was achieved in fig. 3.5c and fig. 3.5d [75].

Laser power also enables to some degree melt pool control, as observable in fig. 3.6, which directly relate to microstructure tuning. Since it affects heat flow, thus, solidification directions can be modified to some extent. Flat and wide melt pool shape result in columnar grains vertically aligned towards the build direction compared to deeper and narrow shapes, which result in disaligned columnar grains as observable in fig. 3.6b [7].

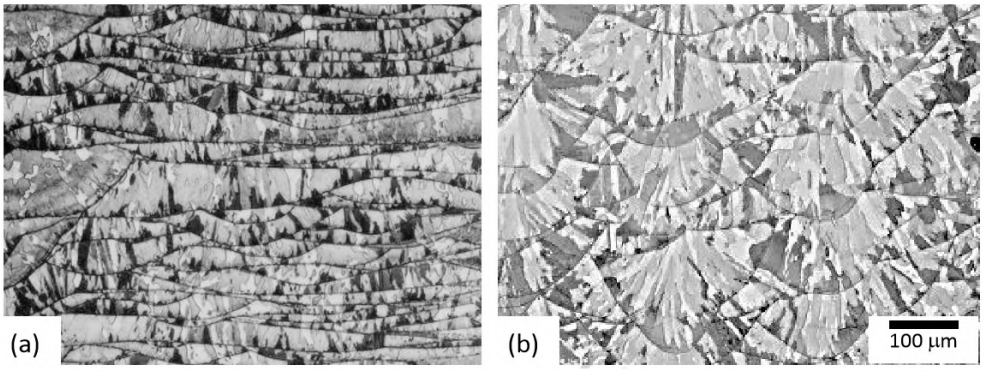

Figure 3.6. Metallography of longitudinal cross sections of SS316L samples printed at 300 mm/s with a laser power of (a) 380 *W* and (b) 200 *W*. The build direction is from bottom up [7].

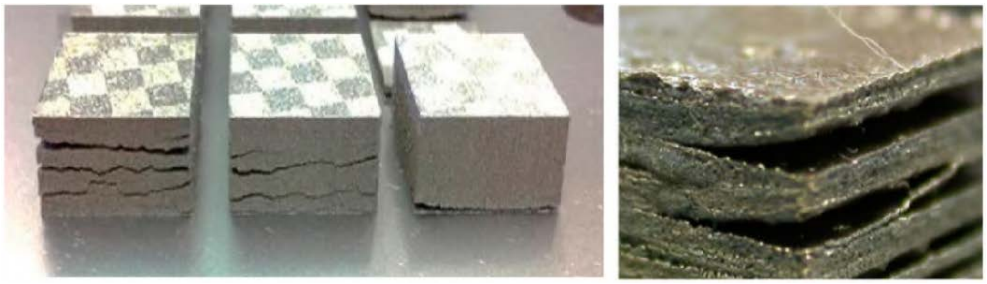

Figure 3.7. Example of delamination defects in PBF process [57].

3.3 LAYER THICKNESS

The thickness of the layer seems to affect the density of the fabricated parts and is often taken into account in combination with factors such as the laser power and the flowability of the powder [6]. Further, it has a major influence when it comes to avoid delamination, defined as the separation of adjacent layers within parts as fig. 3.7 illustrate below. Delamination is commonly caused by incomplete melting between consecutive layers which may occur due to insufficient re-melting of underlying material. While lack of fusion defects are usually localised and can be mitigated by other post-process such has hot isostatic pressing, delamination result in macroscopic defect that cause irreversible damage to the printed object [57]. Accurate tuning of the layer thickness can enable the melting of several material layers and achieve good adhesion between consecutive scans.

3.4 FEEDSTOCK QUALITY

The quality of the powder is determined by size, shape, surface morphology, composition and amount of internal porosity. This factors influence physical variables such as flowability, how well a powder flow and apparent density, how well a powder packs. These characteristics influence the powder layer density, thus playing a decisive role in the density of final parts and related part properties [6]. Fine particles typically improve apparent density since they fit in the interstitial space between larger particles, but they also reduce flowability. Powder production technique directly relate to their quality, since different techniques result in distinct particles shapes which then affects physical variables; for example, spherical particles present higher flowability and apparent density than highly distorted one. In addition to that, depending on the production technique, inert gasses can be entrapped during the production and transferred to the printed part, due to rapid solidification, which would result in powder-induced. It must be said that a wider particle size distribution generally results in higher density and surface finish of the fabricated part. However, smaller powder particles cost more as a feedstock than larger size range, which makes the choice of high quality feedstock powder not always the best parameter in order to achieve the desired quality of the fabricated part [57].

Although, recent studies focused on understanding how feedstock properties change with reuse, since AM technology permits it, thus increasing the efficiency while addressing the lack of consistency in powder feedstock, which is a common problem of the process. fig. 3.8 shows the feedstock for virgin and reused state, in which both present nm to µm-sized satellites. In recycled particles it is possible to observe a general increase in irregularity and no visible boundaries on the surface. Few reused particles, indicated in the bottom images of fig. 3.8, are smoother and more spherical compared to others, suggesting that during the process thermally affected particles undergoes re-solidification which removed the rough surface.

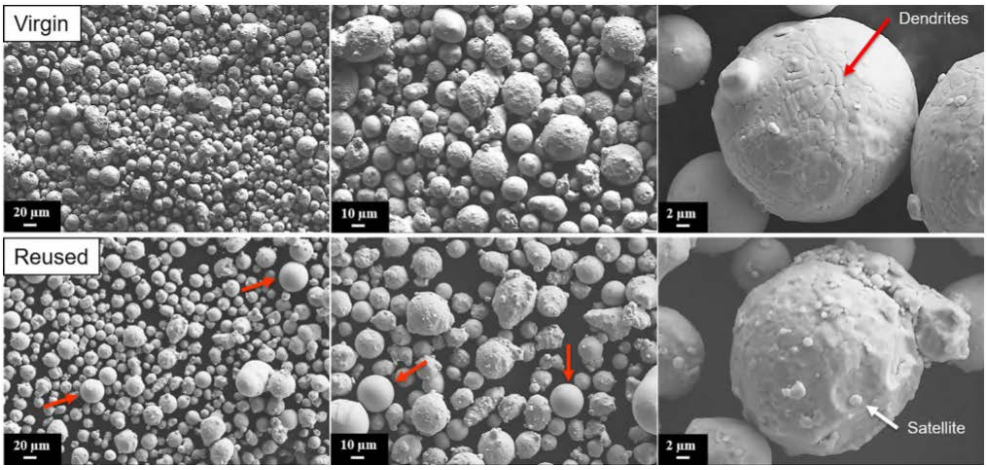

Figure 3.8. SEM images of 316L powders at different magnications [22].

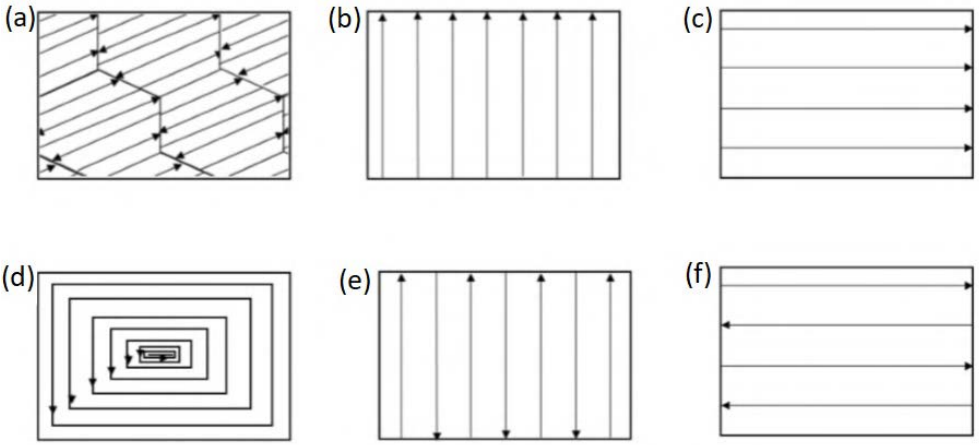

Figure 3.9. Schematic representation of various scan patterns: (a) hexagonal; (b) vertical concurrent; (c) horizontal concurrent; (d) concentric; (e) vertical countercurrent; (f) horizontal coundercurrent [36].

3.5 SCAN STRATEGY

The scan strategy refers to the path that the laser beam follows during the building of each layer. Several pattern has been developed and examples are illustrated in the fig. 3.9 below. The reason behind different scan pattern usage is related to their ability to enable the dissipation of the heat generated by previous passes; thus enable a certain degree of control over the resulting microstructure. In fact, a deposition pattern that rotates by 90° every layer can effectively reduce the formation of dendrites in the build direction [40]. Moreover, scan strategy has an influence on process parameters, since for each strategy laser power and velocity need to be optimised [57].

Part II

MATERIALS AND METHODS

4 APPROACH TO EXPERIMENTAL ANALYSIS

In any field, the approach implemented will influence the overall outcomes of the work, in that sense it is good practice define the objectives before even starting a work of any kind. This is particularly true in research field, where a well thought plan can drastically reduce experimental errors, thus leading to overall better and more reliable results.

In additive manufacturing of metals many factor influence each other and their resulting effects, thus strongly increasing the process complexity. It has already been mentioned that during L-PBF process of SS316L, hierarchical microstructures made by ultrafine grains in the order of few microns can be observed (see chapter 3). Therefore, it is believed necessary to have a preliminary idea of the printing's results to being able to isolate and compare the parameter's effects considered in the present work.

4.1 SAMPLES' GEOMETRY

During L-PBF process transfer of heat can occur in different ways that need to be considered (see section 3.1). With that in mind, part's geometry and shape play an important role in determining the magnitude of the different heat's transfers. For example, the geometry will affect the thermal insulating effect of the metal powder surrounding the part, indirectly leading to various thermal gradient during printing depending also on the thickness of the fabricated part. It must be said that is no simple task being able to clearly isolate the geometric factor effect from the rest of the parameters that intervene during the process affecting the heat's transfers. Nonetheless, the primary assumption made in this work is that even a simple, small dif-

ference can potentially lead to a visible difference. Hence, the geometries selected for the parts had to be simple, and differ from each other enough to enable any possible change to be correlated by a measurable quantity. Therefore, the geometries taken in consideration in the project are cylindrical and conical shape. The difference in cross sectional area of the parts should result in dierent heat extraction, thus aecting to some extent the microstructure. Moreover, the printed samples exhibit the same dimensions, in terms of diameter and height which enable univocal correlation to the geometric factor.

The two different geometry were first design with the licensed software AutoCAD 2019 and subsequently exported in .stl files reported below in fig. 4.1. The main dimensions are 40 x 60 mm^2 diameter and height respectively, in this way the conical shape would have enough surface at the highest cut to permit the analysis (for more details see section 6.1).It is good practice to check the designed parts for integrity before printing in order to avoid any problem related to the geometry to arise during the printing process. Hence, for this purpose open source software Meshmixer has been used, even if not required since the geometries were appositely chosen to be simple. A photo of the second series (i.e. 65 W laser power) consisting of a cylinder and a cone can be seen in fig. 4.2. More detail regarding the printing's setting chosen for the parts and their nomenclature will be given in section 4.3.

4.2 SELECTION OF THE PARAMETERS

In order to investigate what parameters can be best for a certain material a common approach is the use of models that give an approximation of what is expected to be found in the process. This also reduce the possibility of errors while printing the parts. Therefore, a simple analytical model able to get more insight on the relation between the main process parameters and melt pool geometry was implemented in a spreadsheet [53]. The mode

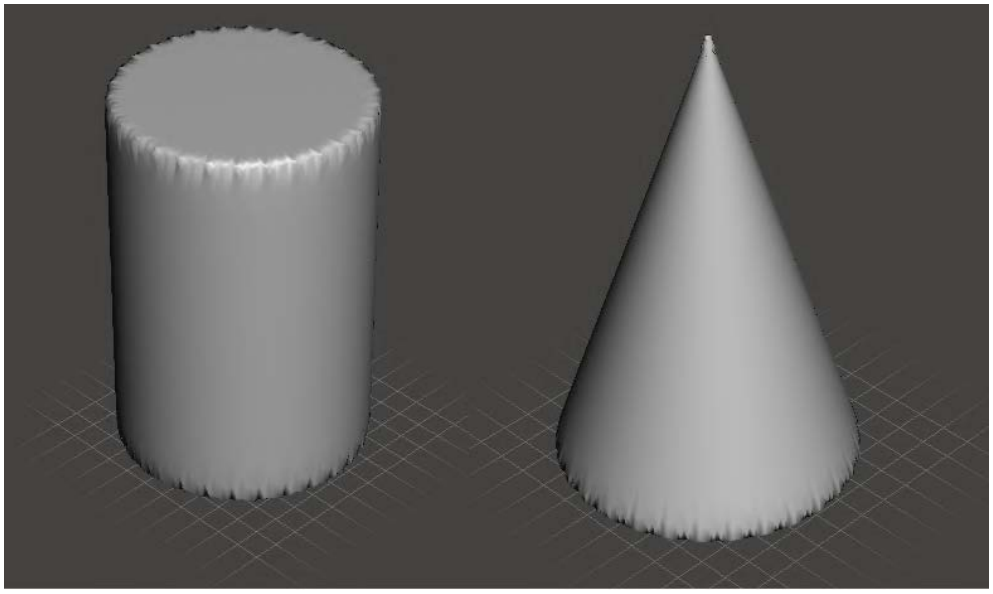

Figure 4.1. Design of the two different geometries exported in.stl file.

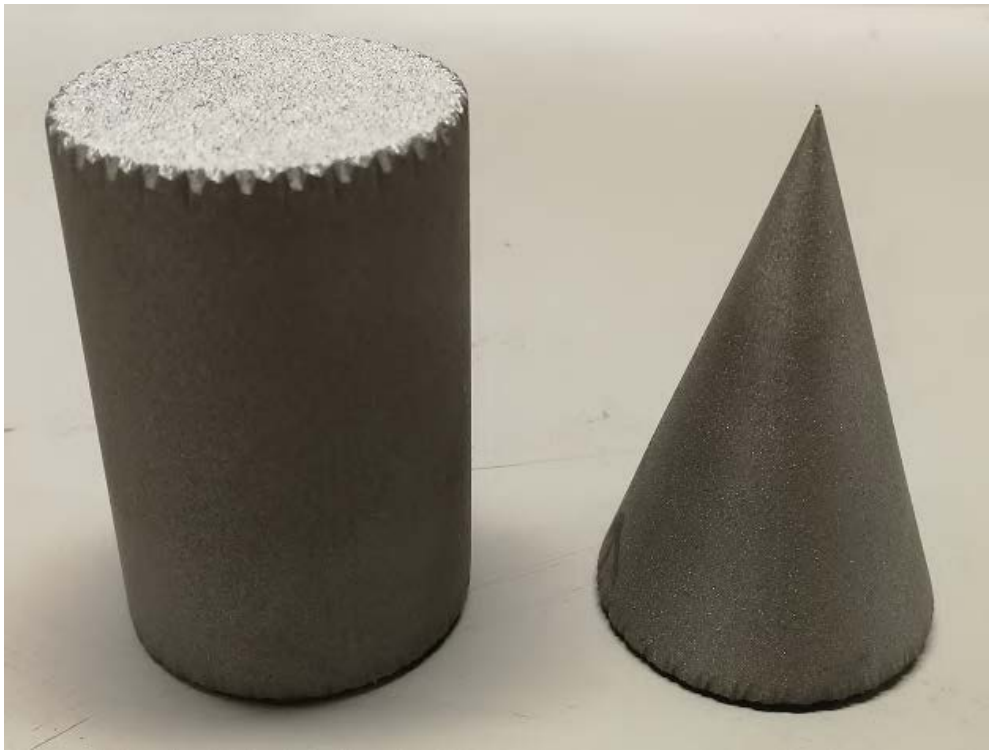

Figure 4.2. Photo of the second series samples.

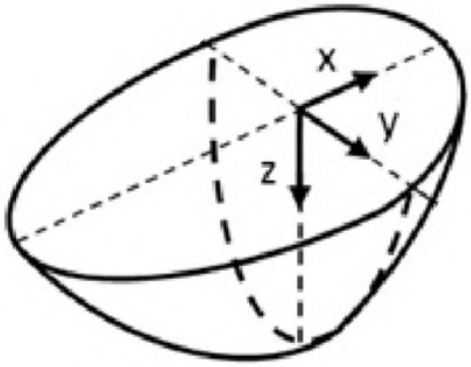

Figure 4.3. Schematic illustration of the melt pool shape highlighting the reference axis used in the model implemented in this work.

presented, based on the Eagar-Tsai thermal model, assume a regime where the powder is already melted and the surface of the liquid is flat. The thermal conductivity of the powder is smaller compared to the substrate, which will result in a shorter time to melt the powder [12]. This relate to the fact that the powder present higher absorptivity than the melted surface, and it consists of relatively isolated powder particles with small heat capacity [5]. Then, higher amount of energy and longer time are required to melt the substrate material once good thermal contact is established. Moreover, the heat of fusion for a metal is small if compared with the energy required to heat the same material to the melting temperature. Hence, it won't affect the temperature distribution and can be ignored [15].

The laser's shape has been considered as Gaussian beam, scanning the substrate along with the x direction. While y is directed in the transverse direction, and z is the coordinate normal to the substrate surface. An illustration of the resultant melt pool is depicted in fig. 4.3; thus, its length, width and depth lies on the x, y and z directions respectively. In eq. (4.1), two dimensionless parameters are defined: p is the ratio of the laser dwell time to the thermal diffusion time; and B, the ratio of the laser deposited energy density to the melt enthalpy h_s.

$$p = \frac{D}{ua} \qquad B = \frac{AP}{\pi h_s \sqrt{\pi D u a^3}} \tag{4.1}$$

Where u is the scan velocity, a refers to the beam radius, absorptivity is A, laser power is P. The properties in table 4.1 have been calculated at the room temperature Tr = 298 K since analysis in which temperature dependent properties were implemented exhibited non-significant differences [53]. Furthermore, some studies have found that the properties at room temperature give the best agreement with the observed melt pool dimensions for laser powder bed fusion [60]. The melting temperature of SS316L has been obtained as the average of the liquidus and solidus temperatures; thus $T_m = 1678\,K$ [47]. While, the thermal diffusivity D and melt enthalpy h_s has been obtained by its definition in which k is the thermal conductivity, C refers to heat capacity and ρ to the density as table 4.1 outline. The value of the melt enthalpy assumed in the calculation is $h_s = 9.8\ kJ/cm^3$ [53]. The absorptivity is defined as the fraction of the laser power absorbed by the material and for the following calculations it has been assumed a value of $A = 0.3$, as it is a common literature value for SS316L [19, 32]. Although, the absorptivity is expected to be affected by other factors such as processing parameters (laser power and scan velocity), melt pool surface roughness, oxide coverage and gas composition above the melt pool; in the present work it was assumed constant during the process.

Table 4.1. Thermo-physical properties of AISI 316L steel [66].

Density (Kg/m^3)	$\rho = 7921–0.614T_r + 0.00002{T_r}^2$
Thermal conductivity (W/mK)	$k = 14.307 + 0.0181T_r–0.000006{T_r}^2$
Heat capacity (J/KgK)	$C = 444.79 + 0.5807T_r–0.001{T_r}^2 + 7 \cdot 10^{-7}{T_r}^3$
Thermal diffusivity (m^2/s)	$D = k/\rho C$
Melt enthalpy (J/m^3)	$h_s = \rho C(T_m - T_r)$

Three universal functions can be defined and correlated only to B and p; their complete formulas are reported below in eqs. eq. (4.2), eq. (4.3) and eq. (4.4).

$$S(B,p) = \frac{1}{\sqrt{p}}[0.008 - 0.0048B - 0.047p - 0.099Bp + plnp(0.32+ \\ +0.015B) + lnB(0.0056 - 0.8 + 0.29plnp)] \tag{4.2}$$

$$L(B,p) = \frac{1}{p^2}[0.0053 - 0.21p + 1.3p^2 - 1.9p^3 - p^2(-0.11 - 0.17B) + \\ + B(-0.0062 + 0.23p + 0.75p^2)] \tag{4.3}$$

$$(B,p) = \frac{1}{Bp^3}[0.0021 - 0.47p + 0.34p^2 - 1.9p^3 - 0.33p^4 + B(0.00066 + \\ -0.0070p - 0.00059p^2 + 2.8p^3 - 0.12p^4) + B^2(-0.00070 + \\ +0.015p - 0.12p^2 + 0.59p^3 - 0.023p^4) + B^3(0.00001 - \\ +0.00022p + 0.0020p^2 - 0.0085p^3 + 0.0014p^4)] \tag{4.4}$$

Consequently, the melt pool's geometry in terms of melt pool depth d, width w and length l, can be obtained from universal functions S, W, L as eq. (4.5) describe; independently from the material characteristics which have been already taken in consideration in eq. (4.1).

$$d = \sqrt{\frac{Da}{u}} \cdot S(B,p) \qquad w = a \cdot W(B,p) \qquad l = a \cdot L(B,p) \tag{4.5}$$

4.3 PRINTING'S SETTINGS

During the setting's selection phase a lot of attention should be putted in selecting the parameters that are optimal for the printing process while avoiding unwanted situations. Applied to this project, the key aspects considered were: avoid key-holing effects and other defects such as warping, porosity and residual stresses. On the other hand, the selected parameters should have guaranteed good adhesion between consecutive layers, thus achieving a melt pool's depth higher than the nominal layer thickness, without reaching the key-hole mode that would lead to bigger pores caused by the entrapped gasses. Therefore, using the outputs of the model combined

with the expertise of the I-Form researchers, it was possible to select the optimal parameters successively used to print the samples.

In order to reduce the factor's influence between each other that would lead to inconsistency of the obtained result, it has been decided to only modify the laser power between three increasing value level. Laser power, as well as scan velocity, presents a strong influence on the melt pool's depth, thus printing three series of samples each with distinct value of laser power, while maintaining constant the velocity, should isolate the effect of this factor [31]. Nonetheless, a careful selection of the fixed parameters was done, keeping in mind that every parameter has an influence on the process and not optimal values can potentially lead to unwanted situations above mentioned. In fact, to avoid any potential influence, every parts have been built in the same position, namely (x,y) on the building plate; thus, any gas flow effect would be consequence only of the geometry of the sample. Therefore, three series have been printed each consisting of a distinct laser power value and the two geometries above mentioned resulting in six fabricated parts.

As a first approach to the printing process, the parameter's values were selected in a way that one of the three series of prints would almost tap into the key-hole mode. In this way, not only it would enable to investigate the limits of the machine, but also would lead to significant difference between at least one of the series would be obtained. Therefore, when deciding the order of the prints, it has been decided to start with the most critical setting, i.e. the highest laser power value, since it would have higher chances to arise any problem; the machine's settings are summarised in table 4.2.

Table 4.2. Summary of the pilot printing settings.

Scan velocity (mm/s)	Layer thickness (µm)	Hatch spacing (µm)	Laser power (W)	Energy density (J/mm^3)	Depth (µm)	Width (µm)	Length
0.5	25	100	85	68	41.63	89.78	177.42

The critical energy density at which the heat transfer change from conduction mode to key-hole mode seems to vary between printers, as above mentioned (see chapter 3). In the case of the machine used in the present work, the manufacturer's expertise was that key-holing would occurs with volumetric energy densities above 70 J/mm^3 (for further details regarding

the printer used see section 5.2. The results of the pilot printings are presented and discussed in section 7.1

Consequently, optimal finalized parameters were selected and are listed in table 4.3. Minor tweaks of laser power and velocity were done to lessen the overall laser spot exposure. Therefore, it would guarantee the powder's melting mechanism to be controlled by thermal conduction, thus avoid unstable melting during the process. Moreover, it would also decrease the magnitude of spattering behaviours at the time of printing, resulting in less process-induced porosity. Meanwhile, every laser power value would enable the melt of the last printed layer increasing the odds of overall good adhesion in the fabricated parts. A numerical number has been given to each printing series, consisting of both shapes, to be able to univocally refer to one laser power level when discussing the result in chapter 7 and chapter 8. The enumeration started with the most critical parameters sets for the machine; thus, the first printing series refers to the 70 W laser power value.

Table 4.3. Summary of the definitive printing settings.

Scan velocity (mm/s)	Layer thickness (μm)	Hatch spacing (μm)	Laser power (W)	Energy density (J/mm^3)	Depth (μm)	Width (μm)	Length (μm)
0.6	25	100	60	40	28.48	71.87	128.76
			65	43.33	30.09	74.44	138.02
			70	46.67	31.62	76.92	147.28

5 EXPERIMENTAL SETUP

In a good quality work, the display of the results and their discussion are of considerable importance. However, to the same extent a description of the machines and materials used to achieve those results should not be neglected. A detailed list of the experimental setup can enable the repeatability of the work in order to get similar results, thus providing the needed conditions to develop future investigations. Therefore, in this chapter a detailed description of the feedstock powder and technologies used during this project will be given, summarizing their working principles and characteristics.

5.1 FEEDSTOCK MATERIAL

The powder's characteristic such as size, shape, surface morphology highly correlates to the powder flowability and capacity of packing when raked in layers. Thus, influencing the density of the fabricated part which would result in an overall less number of defects i.e. weakness zones. In this project, gas atomized stainless steel 316L powder (Legor Group S.p.A.) in the size range 10÷45 μm was used. In a gas atomization process typically the cooling rate imposed by the gas flow are lower compared to water atomization techniques; thus, the powder particles typically present spherical shape with low surface roughness as fig. 5.1 shows. The powder diameter D_p, where p refers to three different cumulative volumes of particles (p = 10%, 50%, 90%), is respectively: $D_{10} = 18\mu m$, $D_{50} = 28\mu m$, $D_{90} = 40\mu m$. ASTM F3049-14 standard stated that "determining the properties of the feedstock powder used in these processes is a necessary condition for industry's condence in

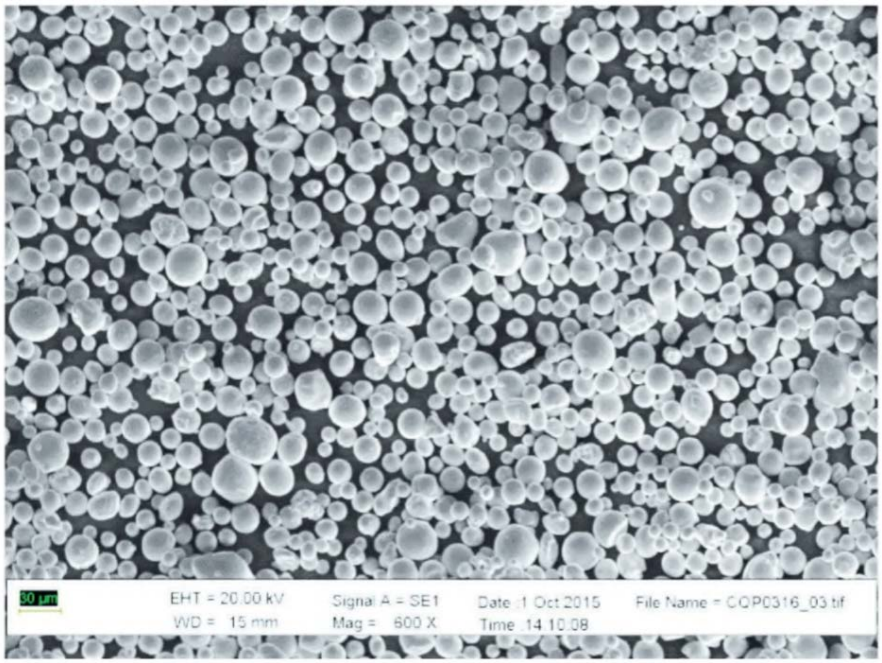

Figure 5.1. SEM image of the gas atomized powder kindly shared by Legor Group S.p.A.

powder selection and ability to produce consistent components with known and predictable properties" [18]. Hence, the chemical composition of the metal powder used in this work is summarized in table 5.1.

Table 5.1. Overall chemical composition of the 316L powder (in wt%).

Cr	Ni	Mo	Mn	Si	P	C	S	Fe
16 - 18	10 - 14	2 - 2.5	0 - 2	0 - 1	0 - 0.045	0 - 0.030	0 - 0.030	Balance

5.2 PRINTING MACHINE

The machine used for the printing belongs to the Mlab cusing series produced by Concept Laser, equipped with Ytterbium fiber able to produce a laser of 100 W. The beam diameter of the machine was fixed to $d = 45\mu m$. This machine is ideal for additive manufacturing, particularly when it comes to small and delicate components with superior surface quality. The built envelope presents a modular structure 90x90x80 mm^3 (x, y, z); thus, appropriate for small parts applications, e.g. in the biomedical or jewellery field.

Table 5.2. Summary of the characteristic of the Mlab Cusing machine.

Build envelope	90x90x80 mm^3 (x,y,z)
Layer system	Fibre laser 100 W (cw)
Layer thickness	$15 \div 50$ μm
Production speed	$1 \div 5$ cm^3/h (depending on material)
Max scanning speed	7 m/s
Focus diameter	45 μm
x/y accuracy	$\pm$ 100 μm
z accuracy	$\pm$ 125 μm
Surface finish	Approx. 5 μm
Power consumption	1.5 kW
Inert gas consumption (Ar or N)	Approx. $0.6 \div 0.8$ l/min
Operatin conditions	Approx. $15 \div 35$

The machine technology follows the ATEX safety directives which enable operations with best safety. In fact, the handling station allows contactless handling of powder right through to the dust-protected removal of components. All processes take place under an inert gas atmosphere of argon. Further, it enables different coordinated exposure strategies to provide maximum level of component quality, in terms of minimizing warping defects or enhancing surface smoothness. Moreover, it offers two different type of coater blades (steel or elastomer based) for different applications. The machine's technical data are summarized in table 5.2, while in fig. 5.2 is reported a photo of the MLab Cusing machine and its envelope.

5.3 OPTICAL MICROSCOPE

The optical microscope (OM) is a well known instrument used in material science to enable the observation at low magnification of structure's features, their arrangement, shape and size. By its definition, it makes use of light as a medium, produced by a lamp, accurately focused and directed by a lens system to the sample's surface. Then, the reflected light is redirected through the eyepiece lens or optical sensor, which further magnify the surface's im-

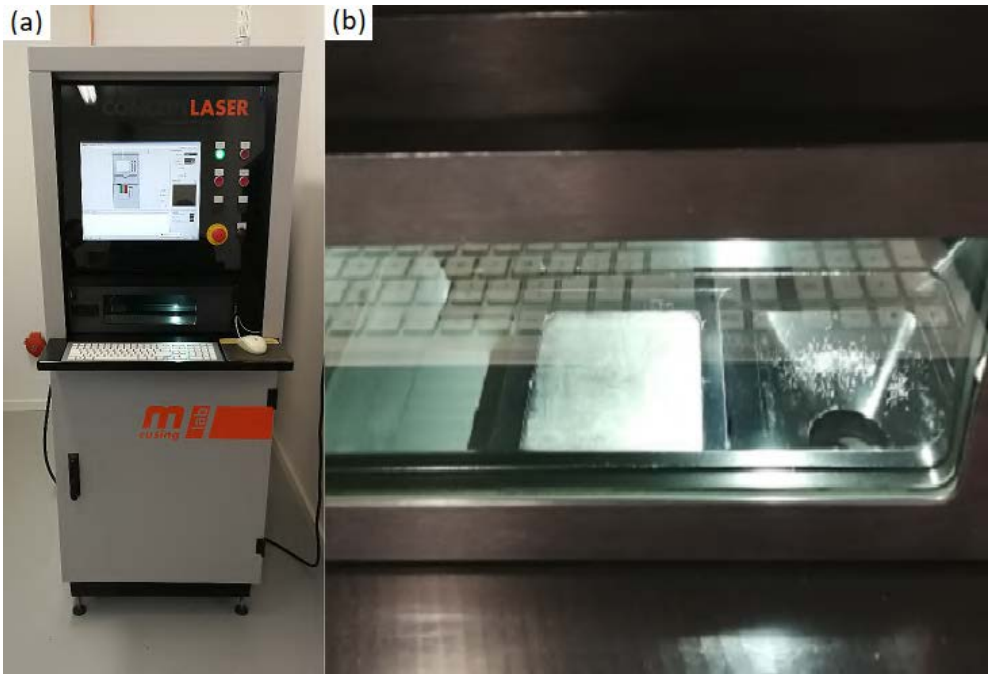

Figure 5.2. (a) Picture of the MLab Cusing machine; (b) building chamber's detail can be seen, in which it dispalys the powder plate, building plate and waste collector from the left to right respectively.

age to be either seen by the viewer or photographed. A schematic illustration is reported below in fig. 5.3a.

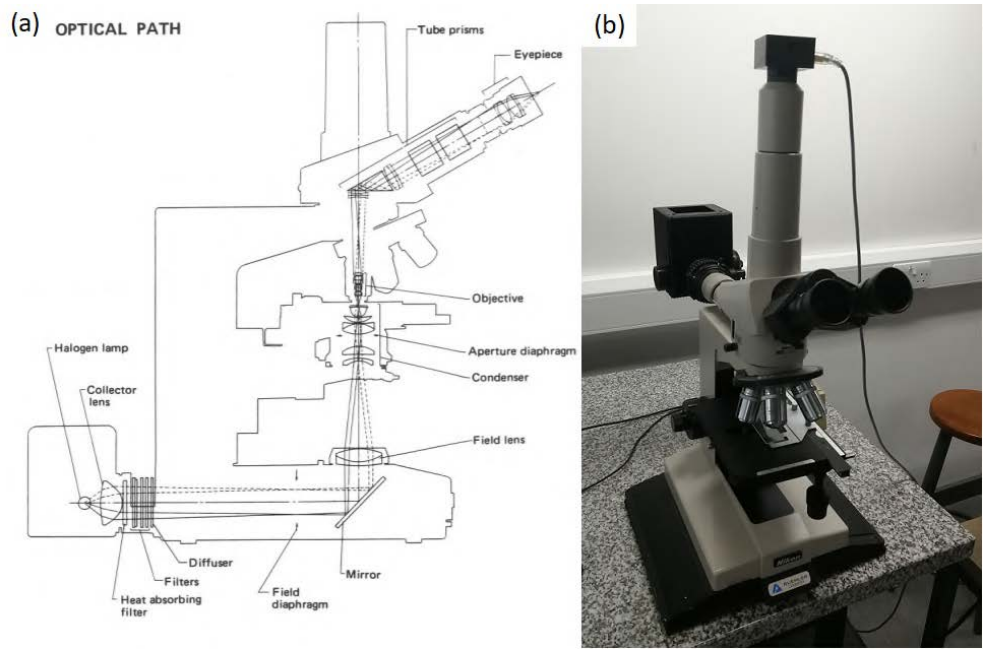

Figure 5.3. (a) Illustration of Nikon Optiphot's optical path from its manual; (b) picture of the Nikon Optiphot Microscope.

In this work optical microscopy analysis on specimens has been conducted with a Nikon Optiphot Microscope. The Optiphot is a durable multi-function

confocal microscope that enables to capture detailed images with the HFX camera. A photo of the instrument can be seen in fig. 5.3b, while some basic features of the Optiphot are:

- HFX Microflex photomicrography system.
- CF Optical system.
- Large rectangular, rotating mechanichal stage.
- 50 w halogen Kohler lighting.

5.4 HARDNESS TESTER

Vickers hardness testers have a wide application in testing metals, especially for making special-purpose tests such as carburized case hardness, maximum hardness of spot welds, high-temperature hardness and fracture toughness of ceramic materials. In this work, Vickers hardness tests has been done with the Mitutoyo AVK-C2 hardness testing machine, presented in fig. 5.4, with the main objective to further investigate the mechanical properties of the surfaces analysed; its characteristic are listed in table 5.3. The tests were done on each printed sample at three specified heights in order to correlate hardness values to the horizontal sections features (see chapter 8).

Table 5.3. Summary of the characteristic of Mitutoyo AVK-C2 hardness testing machine.

Instrument's dimensions	210x58x750 mm^3 (x,y,z)
Resolution of diagonal length of an indentation	1 μm
Specimen dimensions (when using flat anvil)	165x205 mm^2 (y,z)
Main unit mass	Approx. 49 kg
Power supply (main unit)	Approx. 45 W

Figure 5.4. Photo of the Mitutoyo AVK-C2 hardness tester.

6 METHODOLOGY

Along with a list of the instruments used to obtain the discussed results, it obviously necessary to describe the implemented methodologies used to reach those results. Therefore, a detailed description of the methods applied during the project is given in this chapter. For an exhaustive presentation, as it is the author belief, more focus will be put on the reasons behind the decisions taken.

6.1 MICROSTRUCTURAL CHARACTERIZATION

The fabricated parts were sectioned both in the transverse and longitudinal section using standard metallographic procedures; a 2D schematic depicting the cuts is given in fig. 6.1. Three transverse cuts were made at different heights believed to be good representation of potential difference in the print's microstructure, and to enable both cross-sectional investigations and hardness tests. Therefore, it has been decided to observe the sections at 20%, 50% and 80% of the total height of the prints, hence 12 mm, 30 mm and 48 mm respectively. The resultant surfaces were named in alphabetical order starting from the bottom: A, B, C respectively. Whereas, the longitudinal cuts were made at the parts rotational axis to enables the observations of melt pool's depth and their microstructural evolution towards the printing direction. Similarly to the sections, to identify each part in a univocal way samples were named with incremental numbers. fig. 6.2 highlights the analysed surfaces depicted with different colours; it also displays the nomenclature used to refer at each sample's surface.

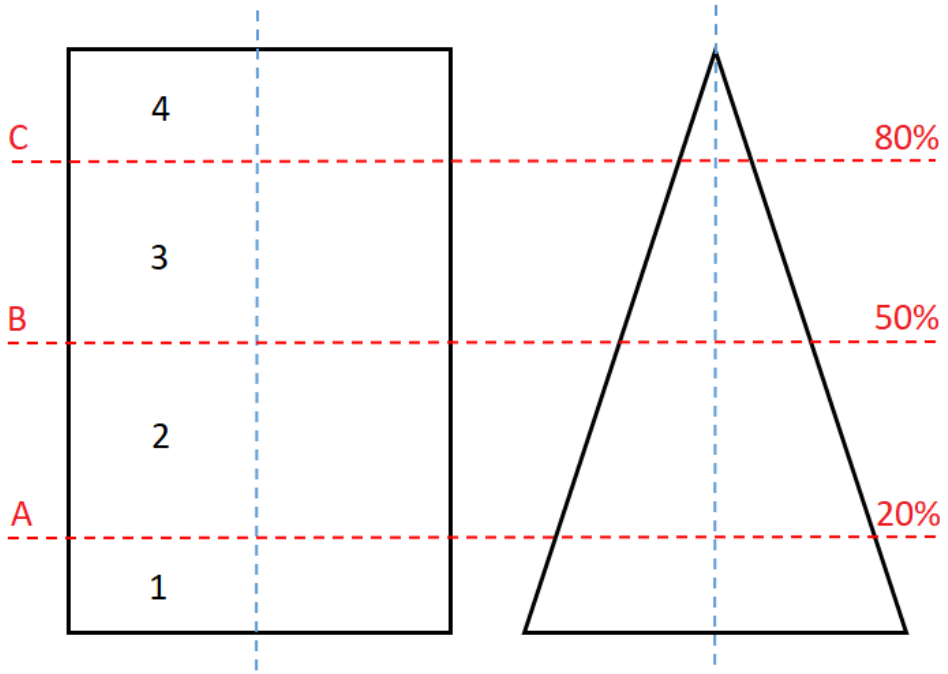

Figure 6.1. Schematic representation of the samples shapes where the cuts are evidenced by dashed lines.

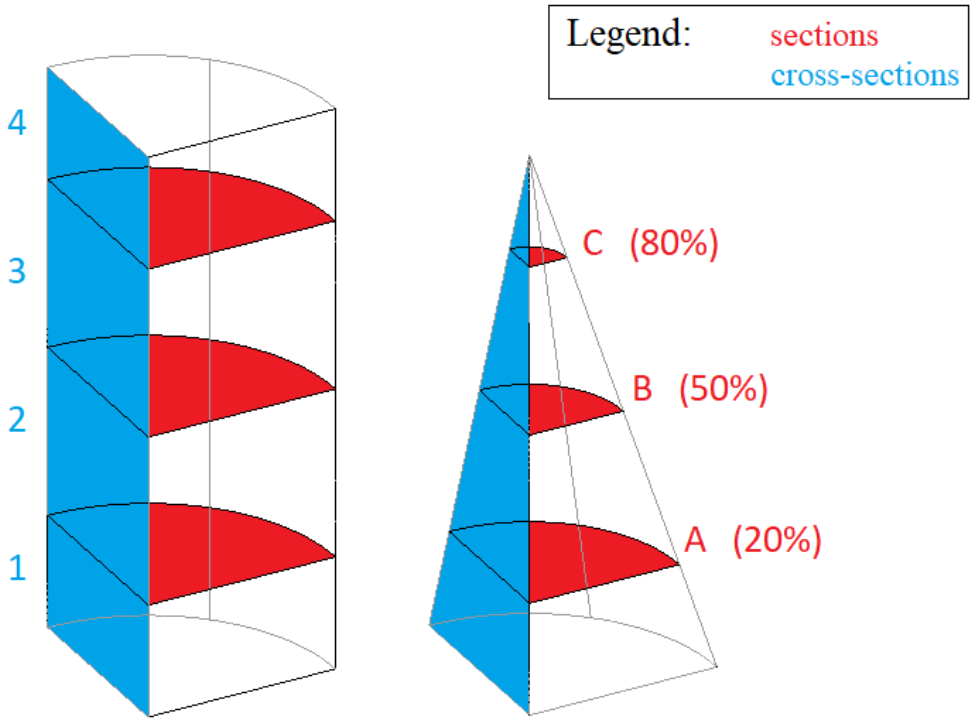

Figure 6.2. 3D illustration highlighting the analysed surfaces and the nomenclature used to distinguish each part.

The SS316L specimens were metallographically prepared for microstructural observation by wet grinding with SiC abrasive papers down to 2500 grit and then polished with diamond paste of 1 μm. A common way found in the literature to reveal anspecimen's microstructure is by using 10% oxalic acid in water as an etchant [7, 46, 69]. However, in the present work an alternative etchant solution, acqua regia, has been found more effective to better reveal the melt pools shape and consisted of 3:1 molar ratio of HCl:HNO_3 in methanol [2, 44, 76].

6.2 MECHANICAL CHARACTERIZATION

It has been decided to use a Vickers hardness tester since the indentation produced would have had a higher difference compared to the Brinell impression; thus, reducing ambiguities when evaluating the measurements. The Vickers test is used as an alternative to the Brinell method to measure the hardness of materials, often is easier to use compared to other hardness tests since the calculations are independent of the size of the indenter.

The basic principle is to observe the metal's ability to resist plastic deformation from a standard source. The Vickers test can be used for all metals and produce a unit of hardness known as the Vickers Pyramid Number (HV), its scale is widely used among hardness tests. In the Vickers hardness test the indenter shape should be capable of producing geometrically similar impressions with well-defined points of measurement combined with high resistance to deformation. Therefore, a square-based pyramid made of diamond is commonly used to satisfy these conditions; its general scheme is reported below in fig. 6.3. It has been decided to use an angle of 136° between plane faces of the indenter tip, since it is the angle that two tangents to the circle at the ends of a chord with a length of 3d/8 produce. This factor origin from the ideal size of a Brinell impression, which was 3/8 of the ball diameter; hence it has been translated to the chord's length that

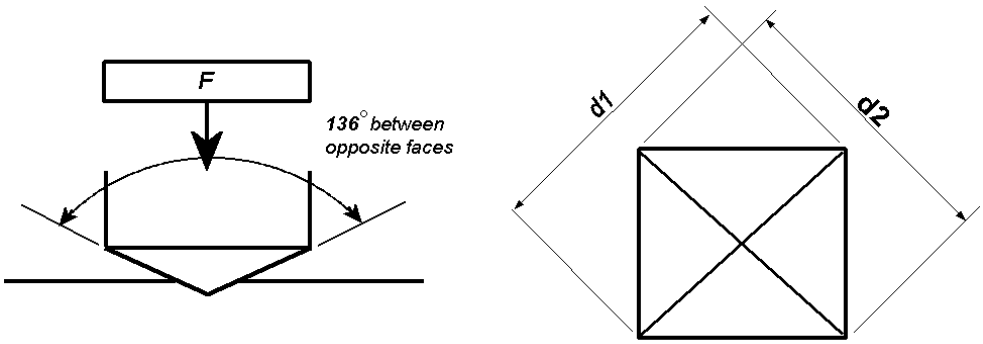

Figure 6.3. Schematic illustration of the Vickers test.

consequently produced the above mentioned angle. The resultant geometry creates an angle of 22° for each face with the horizontal plane.

Accordingly, when a load of known magnitude is applied to a flat surface, depending on the hardness of the material, it will create an impression characterized by the length of the diagonal d. The HV number is then determined by the F/A ratio, as the following formulas describe, where F is the force applied to the diamond and A is the surface area of the resulting indentation [28, 62].

$$A = \frac{d^2}{2\sin(136°/2)} \tag{6.1}$$

$$HV = \frac{F}{A} = \frac{2\sin(136°/2)F}{d^2} \approx 1.8544\frac{F}{d^2} \tag{6.2}$$

Part III

RESULTS AND DISCUSSION

7 MICROSTRUCTURAL CHARACTERIZATION

In this chapter the results of the microstructural characterization will be described and discussed. The melt pools data were measured with the imaging software ImageJ and consisted of 20 sampling per part, which make a total of 80 for each printed sample. All the cross-sectional photos of the samples have been taken to consistently align the building direction from the bottom to the top, as can be also guessed by the melt pools shape in fig. 7.5. It is also important to mention that a selection of representative surfaces has been made in order to highlight and discuss the differences found. The graphs display the mean value of the selected melt pools dimensions combined with the standard error of the dataset from which it has been obtained.

7.1 PILOT PRINT COMPARISON

The pilot print was done at the higher laser power scheduled, i.e. $85\,W$. The relatively low scanning speed lead to an increased laser exposure which resulted in keyholing effect and the presence of carbon by-products identified in the image as dark grey pieces. When condensate starts to form on the building surface it can become included in the part, if the process keeps going, this would generate large voids, inclusions and overall inconsistency in the printing process since for different parts multiple areas of weakness would be found. For this reasons the print was interrupted, a photo of the fabricated part is reported below in fig. 7.1; the incomplete cylinder presented a height of $4\,mm$. It has been decided to analyse its section and

Figure 7.1. Photo of the pilot printing still anchored to the plate in the building chamber.

compare it with the cylinder of the first series, i.e. 70 *W*, which was cut at the same height to enable surface's comparison.

When etched with acqua regia, melt pool boundaries were revealed; in fig. 7.2a, low magnification permits to see the pattern the laser took when printing the part, more over the presence of large jagged pores can be observed, typical indication of keyholing behaviours. Then, fig. 7.2b highlight interesting sub-patterns inside each melt pool; however, they probably are just a result of the etching process due to the use of a particularly aggressive etchant.

The overall view of the 70 *W* cylinder part's structure can be seen in fig. 7.2c and fig. 7.2d. High porosity can be observed and the scan pattern the laser took can be easily guessed. Compared to the cylinder fabricated at 85 *W* laser power, the pores are smaller but more frequent, almost in each consecutive scan. The 70 *W* cylinder was printed with a lower laser power combined with a higher velocity, thus leading to overall lower laser exposure which could have been the cause of such high porosity. Although, it must be said that while at 85 *W* the structure seemed to be less porous, given the same height, it was not able to be printed successfully due to the formation

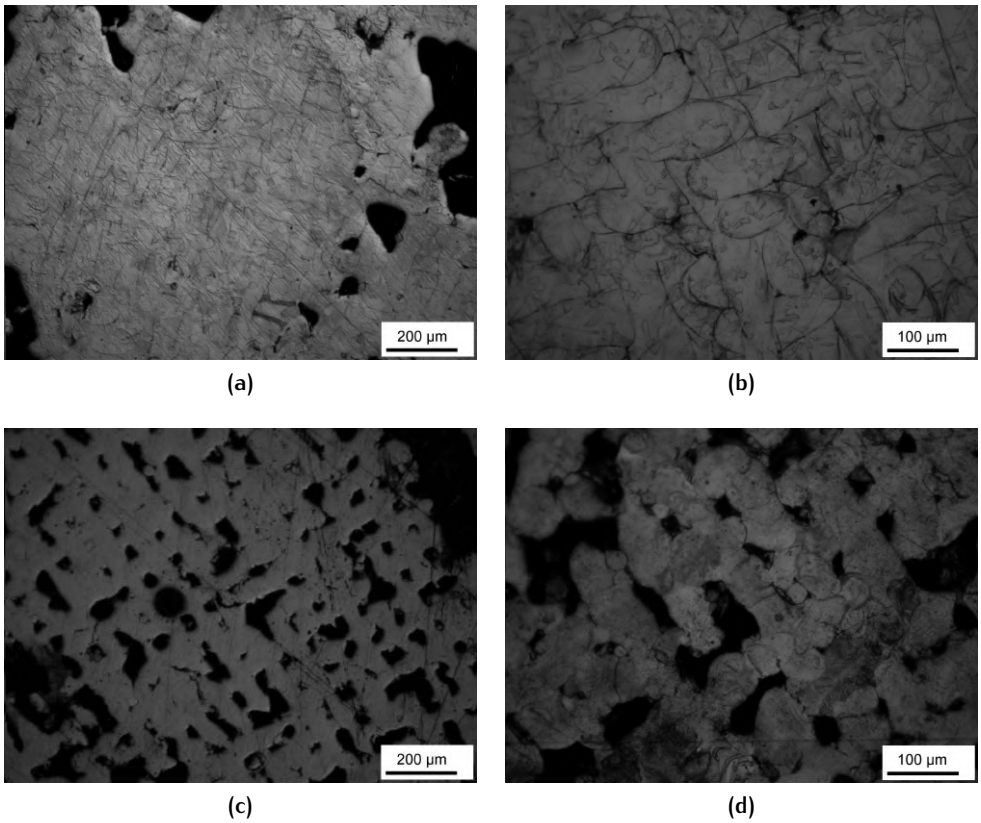

Figure 7.2. Optical microscopies at different magnifications of: (a) & (b) pilot print's section; (c) & (d) 70 *W* cylinder comparison section.

of carbon oxides; needless to say that is the first priority when approaching additive manufacturing.

7.2 EFFECT OF LASER POWER

Optical micrographs of polished cross-sections are shown in fig. 7.3, highlighting porous structure for both cylindrical and conical shape. The cylinders exhibit denser zone separated by vertical column of high porosity, most certainly caused by the scan pattern alignment during printing. It is already been reported that the combination of scan strategy and hatch spacing strongly affects void structures associated with powder denudation effects [42]. Although this is true for the cylinders, the cones present a remarkable difference in pore's positions which will be discussed later (see section 8.2. Overall, 65 *W* series presented the higher density, as displayed in fig. 7.3c,

fig. 7.3d and fig. 7.4b, sign that the process parameters were best optimized. The majority of pores present large crevices of asymmetric shapes, implying they are 'lack of melting' defects caused by the low laser power levels used for printing. SS316L is also more prone to the formation of this type of defects due to its high thermal conductivity which correlates to the formation of the melt pools [44]. Moreover, the absorptivity of the power may has decreased since lower laser powers may imply a less likelihood powder ablation and plasma formation at the surface of the powder bed. Therefore, the large caves are formed with many half-melted particles inside [17].

In fig. 7.4 is possible to observe the effect of laser power on the same height; it is clear that the second series present a less porous surface. Indeed, difficulties had arisen while cutting the samples for the metallographic preparations as the abrasive saw almost blocked during the vertical cutting of the sample. Although still present, the pores are much finer,feature that can only be related to the laser power difference; thus, it is of remarkable importance since every other parameter has not been modified while printing the other cylinders. While 65 W result in the highest density, both 65 W and 60 W laser power levels do not present spattered particles as opposed to the 70 W print. Further, this phenomenon is more marked at the higher heights, thus implying a lower heat extraction capacity at that point caused by an incremental accumulation of heat in lower layers. The spattered particles are usually an indication of the Marangoni effect, where the incident energy is able to melt the powder surface and heat it over the boiling point; hence, leading to vapour recoil momentum which could have further drove the melt outward generating small solidified particles along the laser scans [42]. Although, the parameters were selected to enable a controlled print, thus thermal conduction mode, it is possible that the 70 W laser power tapped into the keyhole mode at certain critical points. It is known that at the end of scan tracks or turning point where laser reverses its direction or when deceleration occurs, it could lead to excessive heat deposited into the powder bed [7, 63].

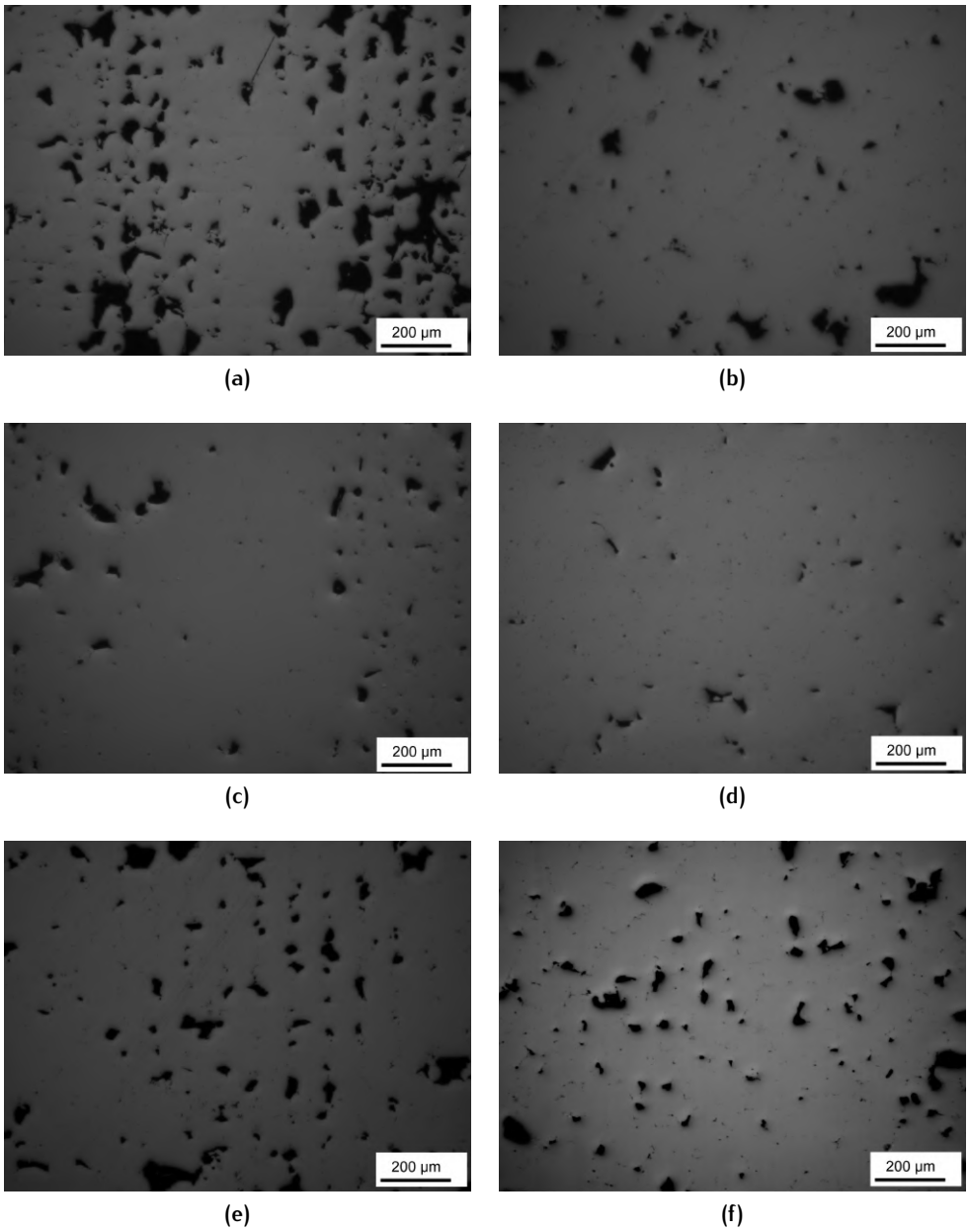

Figure 7.3. Part 3 cross-sectional views of: (a) 70 *W* cylinder; (b) 70 *W* cone; (c) 65 *W* cylinder; (d) 65 *W* cone; (e) 60 *W* cylinder; (f) 60 *W* cone.

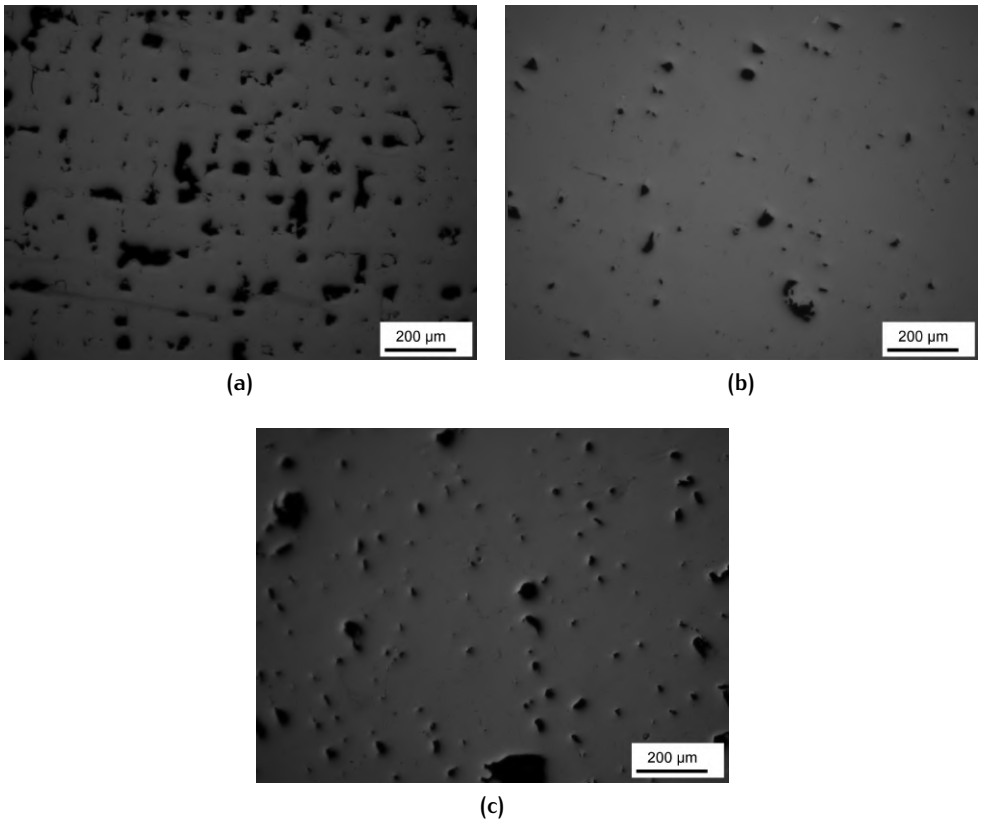

Figure 7.4. Cylinder's sections C microscopies respectively at: (a) 70 *W*; (b) 65 *W*; (c) 60 *W*.

In fig. 7.5 are reported the etched cross-sections of the conical shape at the same height produced with different laser power values used as a representative sample. Due to the high specimen's porosity, etching was difficult and the pictures displayed may not be of best quality. Moreover, an aggressive chemical solution was necessary to etch stainless steel, thus increasing the difficulty of proper metallographic images. Nonetheless, fig. 7.5 shows successful etches of parts of the same height at different laser power levels. It is possible to observe a general reduction of melt pools depths, especially marked between fig. 7.5a and fig. 7.5c also confirmed with the data measured in ImageJ and displayed in fig. 7.6. Although this result is in accordance with the implemented model and other works found in the literature; it is opposed to what Choo et al. found with higher laser power used, in which increasing the laser power seemed to decrease the melt pools depths [7, 17, 53].

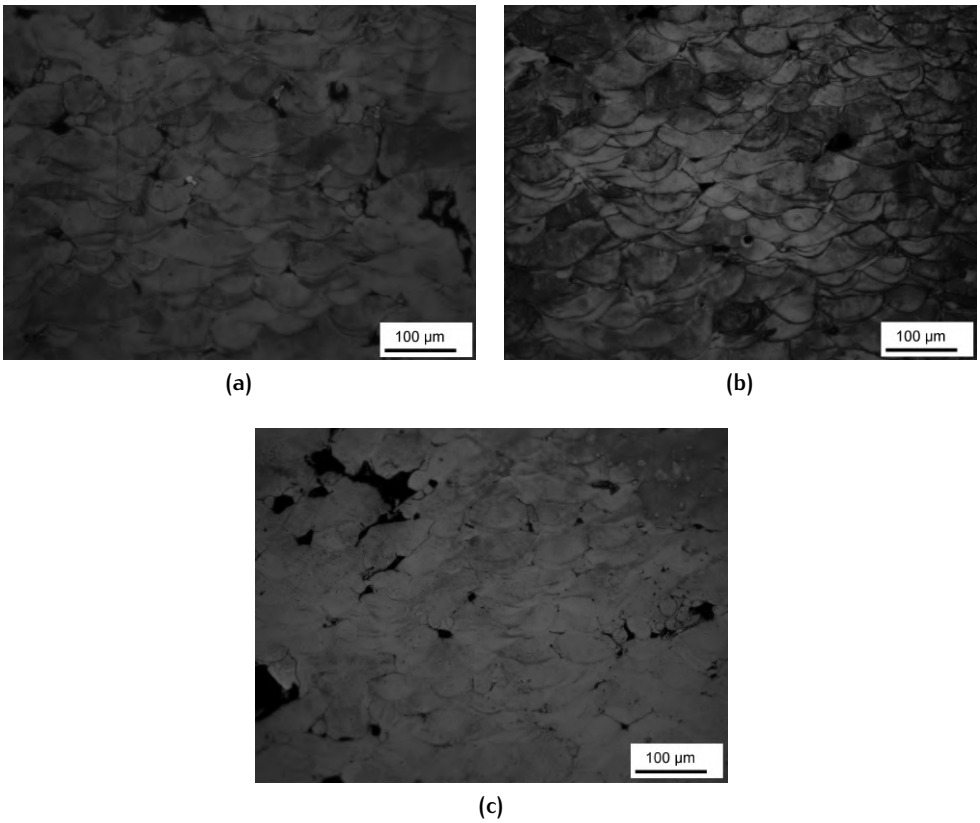

Figure 7.5. Optical microscopies of part 2 etched cross-sections respectively of: (a) 70 *W* cone; (b) 65 *W* cone; (c) 60 *W* cone.

7.2.1 Experimental data

The graphs in fig. 7.6 plot the melt pools depths for each sample properly divided with the nomenclature mentioned above (see section 6.1). As a general trend an increase in the laser power result in an increase in the depths. This observation is in accordance with the model implemented to determine the optimal process parameters. Further, the graphs exhibit a downward trend in which the depths decrease with increasing heights. Although, it must be said that 70 *W* cylinder part 1 and 2 were difficult to etch successfully, due to the high porosity; thus, the resulting depth's measurements could have been affected. Nonetheless, the feature found is consistent in all the samples analyzed, and it will be further investigated below section 7.4.

The melt pools widths data were taken at each horizontal surface and are reported in fig. 7.7. The first set of figures display the comparison between the two geometries at the three different laser power, it is possible to ob-

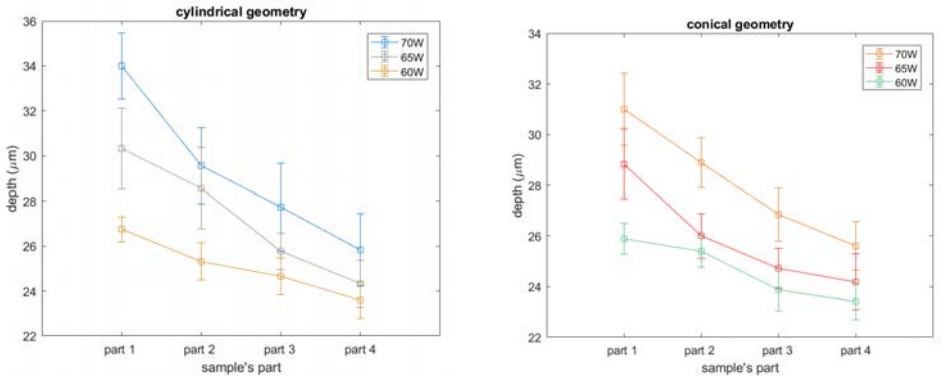

Figure 7.6. Summary of the melt pools depths data from the two different geometries divided by heights.

serve a higher diversity in the cylinder data sets, which span from 44 μ m to 62 μ m, compared to the cone in which the width range is 7 μ m. However, given the high variety, as fig. 7.7 exhibit various different trend, it is not possible to give any accurate statement regarding the influence of laser power on the widths of the melt pools.

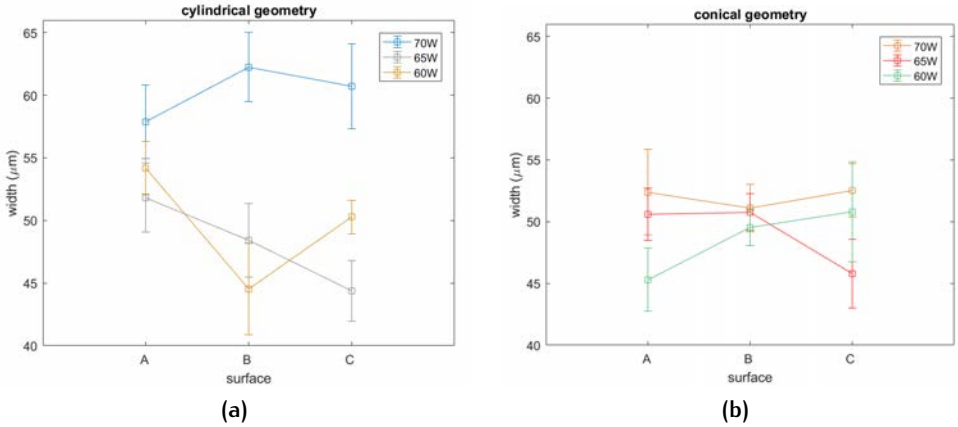

Figure 7.7. Melt pools widths of the two geometries at different sections.

The melt pools lengths are linked to the widths, since they have been measured together while analysing the surface's microscopies. In fact, fig. 7.8 exhibit great variance and different trends can be observed, similarly to fig. 7.7. Nonetheless, a marked difference can be seen in fig. 7.8a between the 70 *W* cylinder and the other two series. This could be the result of the keyholing effect occurring at the highest laser power. However, it seems to only have affected the cylinder of the first series, since the conical shape presented a

less marked trend. Therefore, as it is an effect caused by the geometry, it will be discussed more in details in section 7.3.

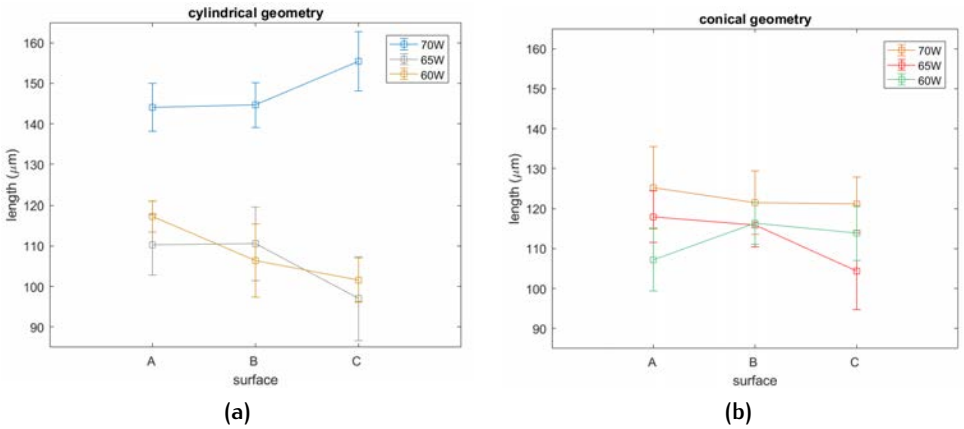

Figure 7.8. Summary of the melt pools lengths data from the two different geometries divided by heights.

7.3 EFFECT OF SAMPLE'S GEOMETRY

In this section, the influence of the sample's geometry is discussed along with the experimental results. It has already been mentioned that the pores' alignment differ between the conical and cylindrical shape, as depicted in fig. 7.3. Moreover, the following figure shows the differences in the surface of the same sample at three different heights; a general trend can be observed. In fig. 7.9a the pores seem to be bigger and more frequent; meanwhile this feature tends to decrease with the height as the other two figures depict. Although pores with comparable dimensions can still be seen in fig. 7.9c, their presence is occasional. This difference has been observed also in the others conical samples and will be further discussed in the hardness tests section (see section 8.2).

Although proper etchings have not been achieved for the reasons already mentioned, fig. 7.10 reports the overall etched structure of the third series samples at the same surface for the purpose of an exhaustive report. In fig. 7.10a and fig. 7.10b, it is possible to observe the pattern the laser took while printing; further, higher number of spattered particles can be seen in

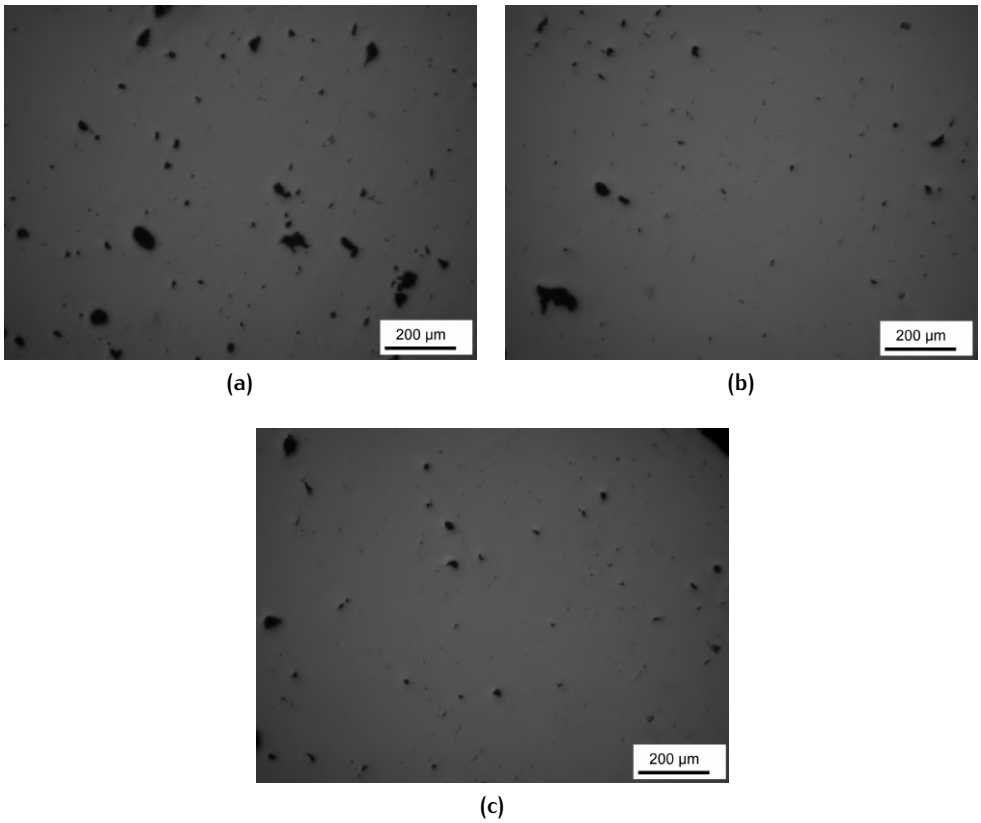

Figure 7.9. Optical microscopies of the 65 *W* cone representing respectively: (a) section A; (b) section B; (c) section C.

fig. 7.10a, similarly to fig. 7.5. Overall, it seems the cylinder present higher melt pools dimensions in both width and length if compared to its the geometric counterparts, as can be also viewed in fig. 7.10c and fig. 7.10d.

Furthermore, the trend found in the plots of fig. 7.6 can also be observed in the pictures of fig. 7.11. The decrease in melt pool depth with the height is related to the accumulation of heat during printing. By increasing the temperature of each built layer, the cooling rates decrease; thus, resulting in a shallower melt pools due to the increased solidification time. A similar phenomenon happens in Ti6Al4V as the increase in temperature gradient, thus higher cooling rates, decrease the dendritic arm spacing [56]. With the exception that SS316L does not present any phase-related change with cooling rate.

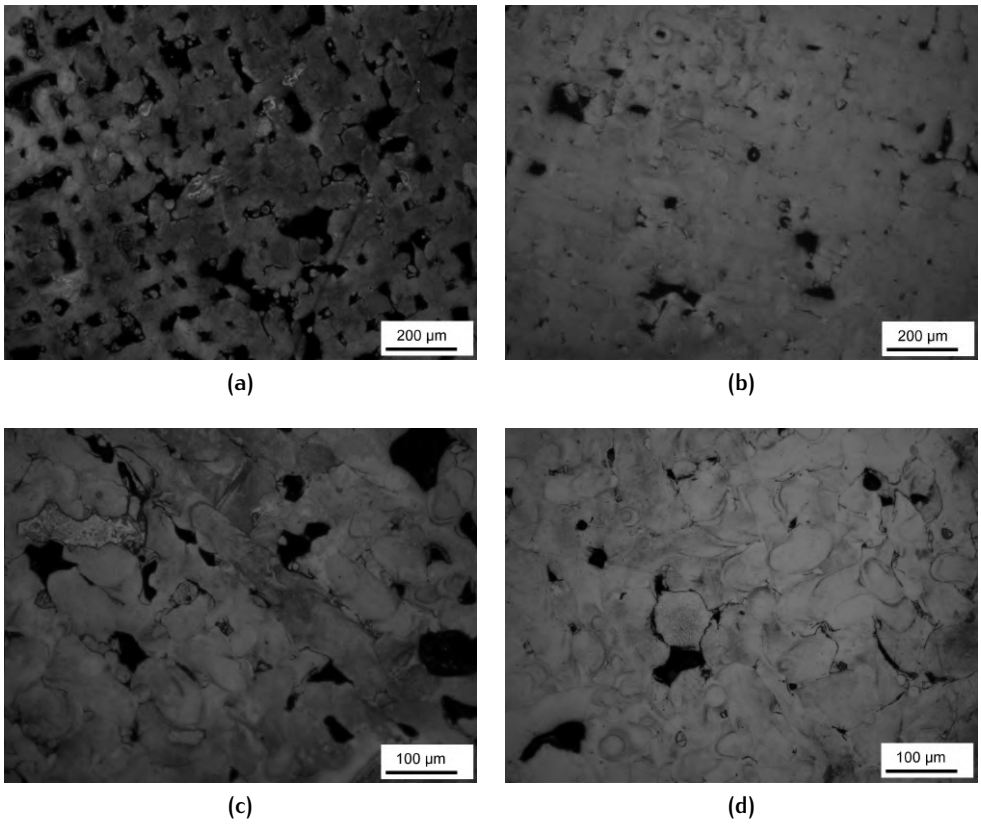

Figure 7.10. Etched surfaces microscopies respectively of: (a) 70 *W* cylinder at section C; (b) 70 *W* cone at section C; (c) 60 *W* cylinder at section A; (d) 60 *W* cone at section A.

7.3.1 Experimental data

fig. 7.12 compare the melt pools depths of each printing series investigating possible correlation between the geometry and the depths. In all the figures, the melt pools depth of the cylinder is higher compared to the conical geometry. However, the difference it is not well defined, with fig. 7.12c part 2 depths presenting similar values. Therefore, further investigations need to be done to better evaluate this correlation (see section 7.4.2. The plots also show the trend already determined in which increasing height result in a decrease of the melt pools depths.

When comparing the melt pools widths of each printed series, a marked difference is displayed between the first series in fig. 7.13a opposed to fig. 7.13b where the geometries present a similar behaviour. Although the two geometries in fig. 7.13c exhibit overall different trends, it must be said that section

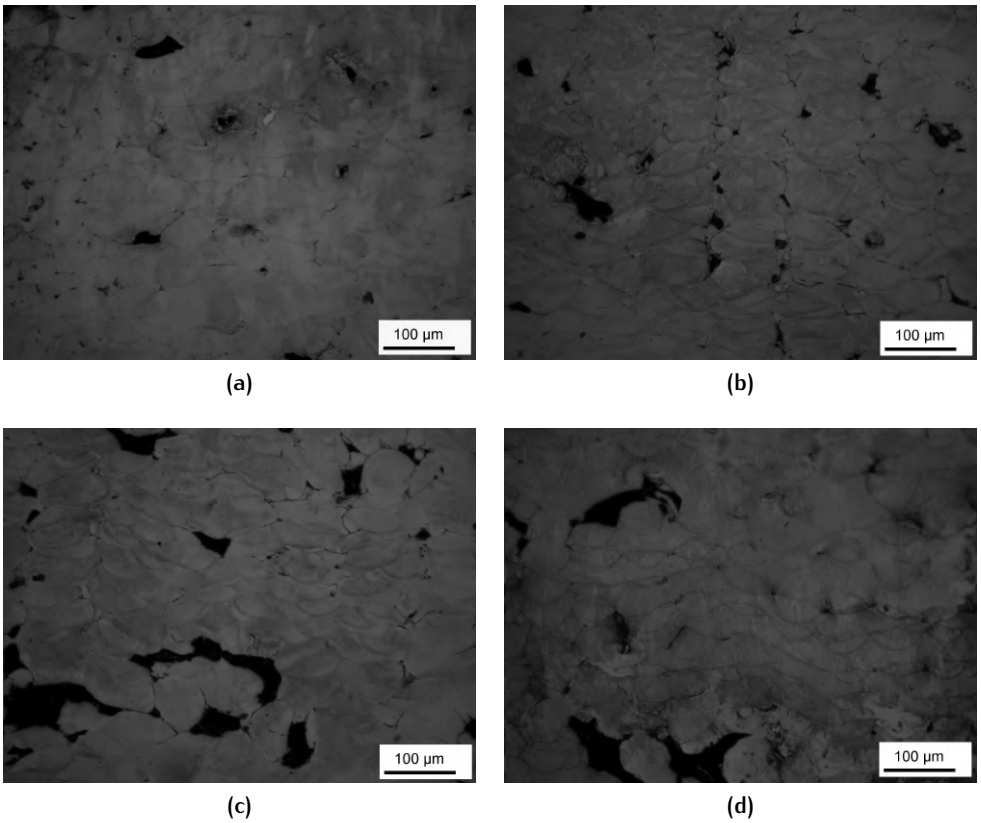

Figure 7.11. 65 *W* cylinder optical microscopies of: (a) part 1; (b) part 2; (c) part 3; (d) part 4.

A of the third series was among the best etches done in this project, as depicted in fig. 7.10c and fig. 7.10d. Therefore, the measurements done on that surface can be assumed more accurate; thus, it enables to state a qualitative influence of the part's geometry on the melt pools widths as follows.

The cylinder presents a reduced heat extraction capacity since the section is constant and the main dissipation of heat can occur either through the bulk materials or the building plate at the bottom. Therefore, as the process goes, each built layer should present a higher temperature than its previous, surely higher compared to the same built layer in the cone, where the reduction in section influence the magnitude of the accumulated heat. It is possible that the temperature difference result in an expanded melt pools widths in the cylinder compared to the cone, as fig. 7.13a exhibit and section A of fig. 7.13c further suggests. Hence, the cylinder is more influenced than the cone by the process; this would also explain the great variance observed in fig. 7.7a and fig. 7.8a.

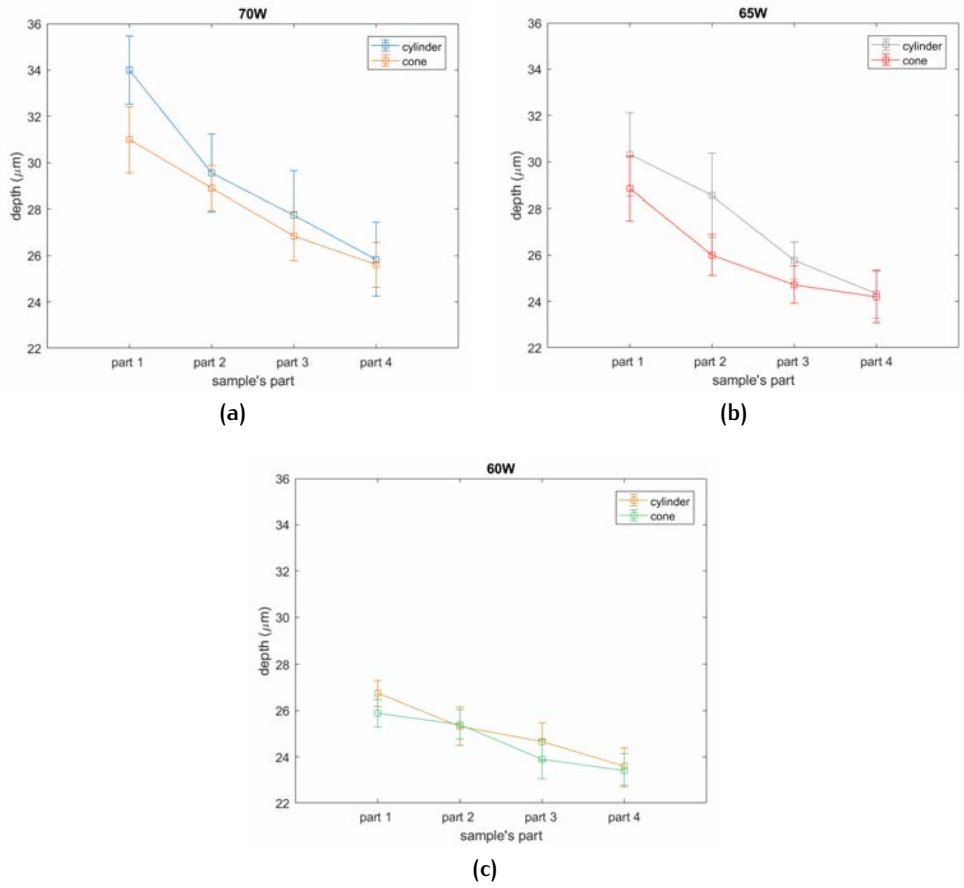

Figure 7.12. Overall melt pools depths divided by geometry of: (a) 70W printing series; (b) 65W printing series; (c) 60W printing series.

Furthermore, similar discussion can be made by looking at the results summarize in fig. 7.14. A significant difference between the geometries of the 70 *W* series is displayed in fig. 7.14a and confirmed by the section A values of fig. 7.14c. This qualitative result is in line with the observation mentioned above. Nonetheless, great variance in both widths and lengths data is present, thus any accurate statement cannot be made. There is the possibility that the geometries displayed too much similarities between each other. Perhaps, a marked difference between the printing's shapes could lead to more consistent observations even in the melt pools' width and length. Although, it also need to be considered that the melt pools' depth is much less dependent on the position of the cut; while the other melt pools dimensions present greater variance even for small variation of the cut's height.

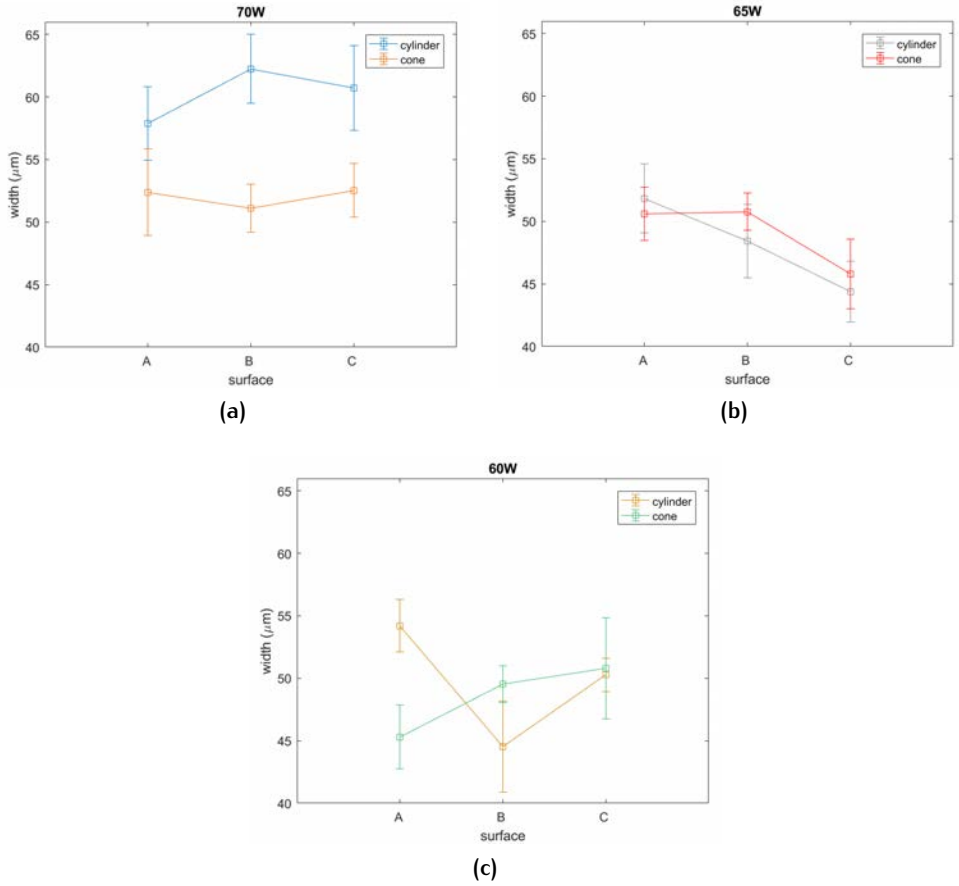

Figure 7.13. Summary of the melt pools widths data divided by geometry of: (a) 70W printing series; (b) 65W printing series; (c) 60W printing series.

7.4 STATISTICAL ANALYSIS

In order to further confirm the observations made in section 7.2, i.e. the decrease in melt pools depths with the height; it has been decided to perform analysis of variance (ANOVA) to confirm there are significant difference among the datasets. All the following figures and tables has been produced using the open source software Rstudio. Below will be discussed the results of the analysis on one representative sample, since similar discussion would have been made for all the other samples. Nonetheless, the analysis assumptions have been validated for each dataset and the summary of the ANOVA tests are listed in the table 7.1 and table 7.2.

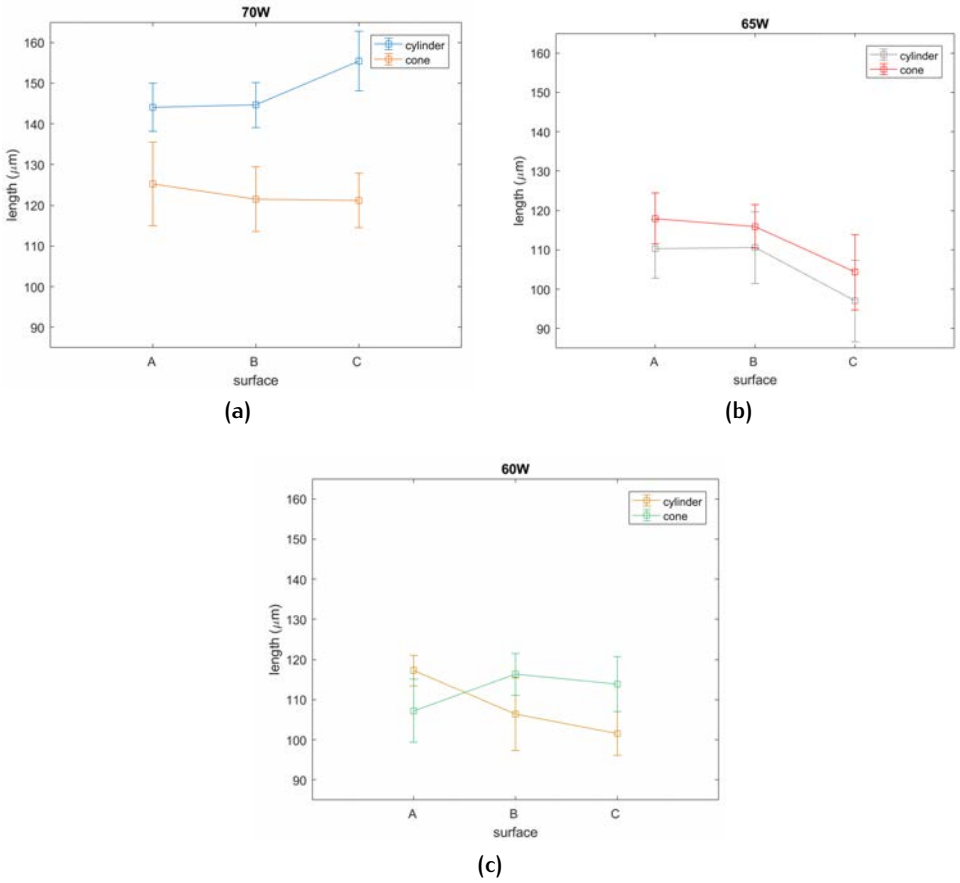

Figure 7.14. Overall the melt pools lengths data divided by geometry of: (a) 70W printing series; (b) 65W printing series; (c) 60W printing series.

7.4.1 Heights comparison

When approaching an ANOVA analysis, there are various assumptions that need to be checked to confirm its validity: the data are normally distributed and the variance across groups are homogeneous. The plots can be seen respectively in fig. 7.15a and fig. 7.15b, and represent the data of the 70 *W* cone. The normality plot shows a satisfactory alignment with the inclined straight line, which represent the perfectly normal distribution. Meanwhile, fig. 7.15b presents the homogeneity of variance validation, that is also met since it exhibits no evident relationships between residuals and fitted values. To better visualize the dataset fig. 7.15c shows the boxplot of the data divided by part, with a black line highlighting the median of each group. Overall, it has been observed the absence of outliers, which are values that are distant from other observations; this indicates that the mean

values have not been affected by them. Therefore, the graphs plotted in this chapter well represent the data for each sample's part.

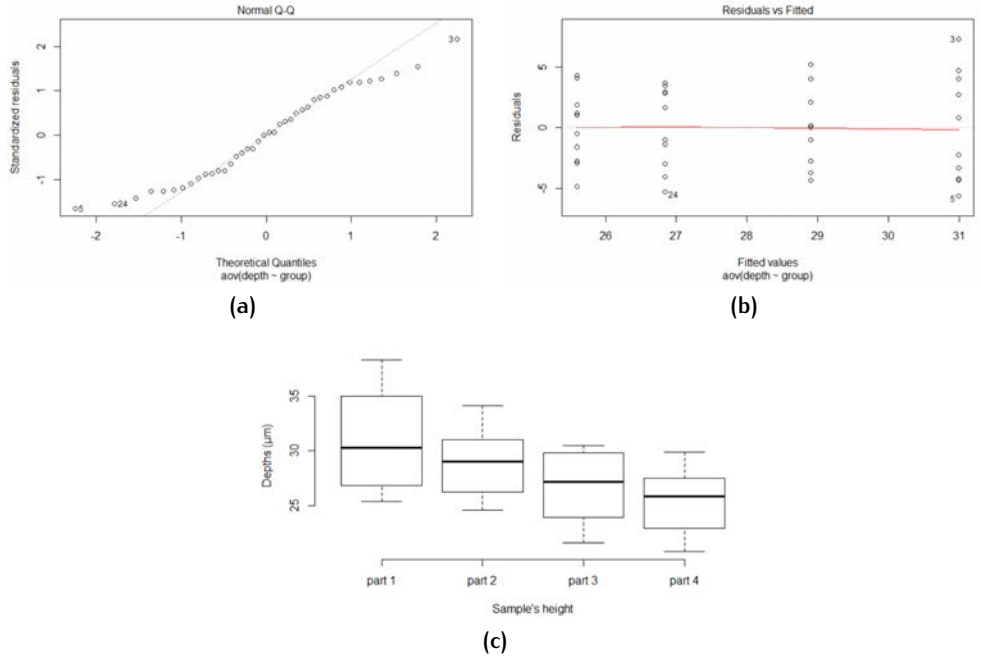

Figure 7.15. Plots representing the data taken from the 70 *W* cone, respectively showing: (a) normality plot of the residuals; (b) homogeneity of variances plot; (c) boxplot to visualize the data.

Below, table 7.1 summarize the ANOVA analysis done on the data gathered at different heights of each sample. An important note is that the degrees of freedom and their residuals were the same for all the samples, respectively: $\mathrm{Df} = 3$ and $\mathrm{R} = 36$, and have been used to calculate the F-value and P-value. The ANOVA results exhibit a statistical significance where the P-values are marked with a star, and the 70 *W* cone presenting a stronger variation compared to the other; hence, there are at least two parts in each sample that differ significantly from each other. The 60 *W* cone does not present a p-value lower than 0.05, however its value is slightly above the threshold; more over the cylinder of the same series present a higher value compared to the other series. A possible answer is that the low laser power used in the third series has a less impact in the depths evolution throughout the sample's height. Overall, the statistical analysis confirm the observation made above regarding the trend between the melt pools depths and the height.

Table 7.1. Results of the one-way ANOVA analysis for each sample.

Sample	Factor	Sum square	Mean square	F-value	P-value
70 *W* cylinder	Depths	366	121.99	4.321	0.0106*
	Residuals	1016	28.23		
70 *W* cone	Depths	168.3	56.09	4.45	0.00928**
	Residuals	453.8	12.61		
65 *W* cylinder	Depths	220.1	73.36	3.556	0.0237*
	Residuals	742.7	20.63		
65 *W* cone	Depths	129.6	43.21	3.779	0.0187*
	Residuals	411.7	11.44		
60 *W* cylinder	Depths	52.18	17.394	3.012	0.0426*
	Residuals	207.87	5.774		
60 *W* cone	Depths	42.06	14.019	2.791	0.0543
	Residuals	180.82	5.023		

The ANOVA test does not give any information on which group present a significance difference between the other; thus, with degrees of freedom higher than two, further analysis have to be made. Therefore, a Tukey test has been performed on the sample's datasets, the summary for the 70 *W* cone is reported in table 7.2. The multiple pairwisem comparison between the means of groups enable to find where the statistical significance lies. The results display the difference between the means of the paired groups, the lower and upper end point of the confidence interval, by default at 95%, and the p-value after adjustment for the multiple comparisons. In the representative results of table 7.2, it is clear that the significance difference is between part 1 and 4 since the p-value of the paired group is well below 0.05. The Tukey test presented similar results for all the other samples; exception made for the 65 *W* cone which exhibited a significant difference also between part 1 and 3, with an adjusted p-value of 0.0466.

Table 7.2. Summary of the Tukey HSD test results of the 70 *W* cone.

Paired parts	Difference	Lower end point	Upper end point	Adjusted p-value
2 - 1	-2.09	-6.3663	2.1863	0.5588
3 - 1	-4.15	-8.4263	0.1263	0.0599
4 - 1	-5.39	-9.6663	-1.1137	0.0088*
3 - 2	-2.06	-6.3363	2.2163	0.5705
4 - 2	-3.30	-7.5763	0.9763	0.1795
4 - 3	-1.24	-5.5163	3.0363	0.8626

7.4.2 Geometry comparison

In fig. 7.12 (section 7.3.1) each series has been plotted to compare if the geometry had an influence in the melt pools depths. In this section, statistical analysis will be made to further investigate the possible correlation, however, it has been decided to compare the dataset of the whole sample between each other, rathed than doing the analysis by pairing the sample's parts. Firstly, it would have been dispersive and difficult to summarize in a clear way; more over the plots did not displayed a marked difference in certain parts, especially in fig. 7.12c, which would have resulted in inconsistency of the analysis. Therefore, the sample's boxplots are paired by series and present the population of each sample. A marked difference between the median of the two geometries can be observed in fig. 7.16a, while it seems to lessen in fig. 7.16b and fig. 7.16c.

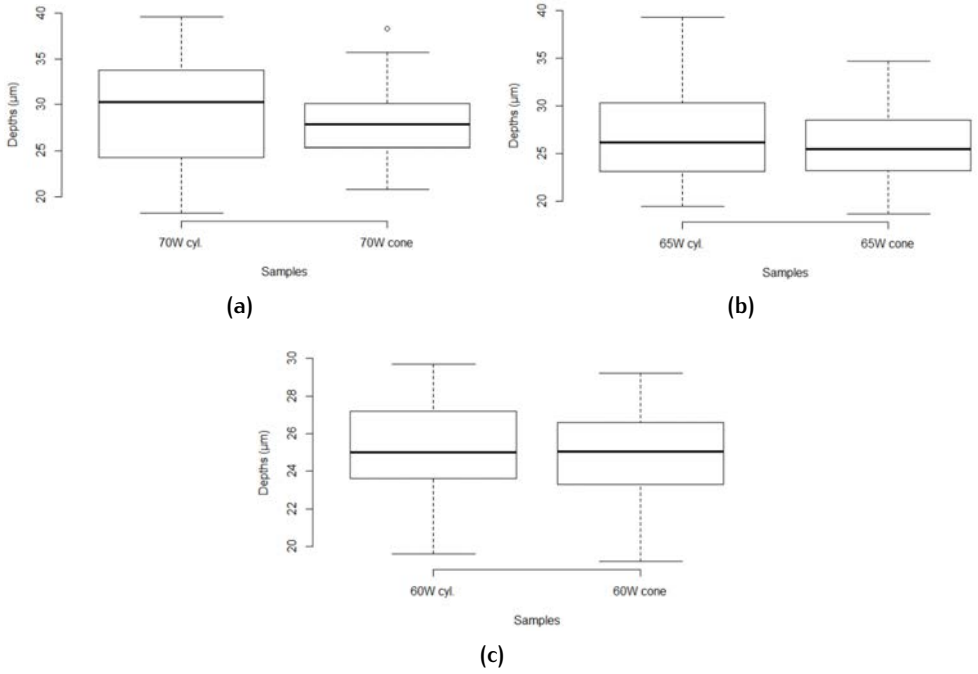

Figure 7.16. Summary of the population of the various samples, respectively: (a) 70 *W* series; (b) 65 *W* series; (c) 60 *W* series.

The summary of the ANOVA tests are listed in the Tab.7.3; all the p-values are above 0.05, thus the outcome is that none of the series present a statistical significant difference in the melt pools depths if compared by geometry. The

second series present the lowest p-value, probably due to the fact that the 65 *W* cylinder's boxplot exhibit a wider distribution, represented by the long whisker in the upward direction.

Table 7.3. Results of the one-way ANOVA analysis for each series.

Sample	Factor	Sum square	Mean square	F-value	P-value
70 *W* series	Depths	28.9	28.92	1.125	0.292
	Residuals	2004.5	25.70		
65 *W* series	Depths	34.1	34.06	1.766	0.188
	Residuals	1504.2	19.28		
60 *W* series	Depths	3.7	3.741	0.604	0.439
	Residuals	482.9	6.191		

8 MECHANICAL CHARACTERIZATION

In this chapter the results of the mechanical characterizations done on the horizontal surfaces are reported and discussed. The Vickers hardness mean values of each sections are displayed in the following graphs along with the standard error of their respective dataset. The data consisted of 5 sampling per surface; thus, making it a total of 15 for each printed part.

8.1 EFFECT OF LASER POWER

The hardness tests results are plotted in fig. 8.1; while the cylinder present highly different values, the cone seems to have a lower diversity for each laser power value used for printing. Although the author tried to do the tests in denser region; it must be taken in consideration the possibility that porosity could have affected the measurements. This is especially true for the $70\,W$ cylinder which presented high porosity levels and, in fact, shows remarkable lower values. Furthermore, a general increase in the Vickers hardness with the increasing height of the analysed surfaces can be clearly seen in all the plots below, especially in the cone geometry. This trend is consistent with fig. 7.9, and it seems to validate the observation already done. $65\,W$ series prints showed the highest density, as depicted in fig. 7.9; this feature is especially highlighted in the cylinders in fig. 8.1a and will be discussed in the next section.

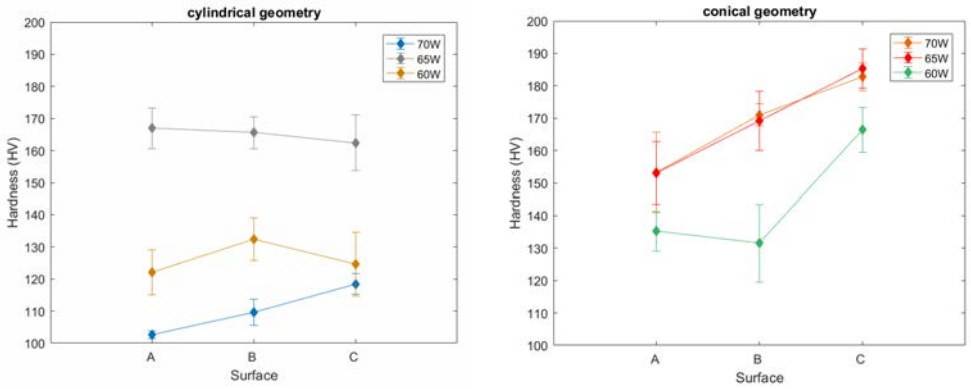

Figure 8.1. Vickers hardness comparison between the two printed geometries.

8.2 EFFECT OF SAMPLE'S GEOMETRY

When comparing each printing series, there seems to be accordance in the hardness values of the two geometries, it is the case of fig. 8.2b and c. However, the first series present a remarkable difference between the two geometries as depicted in fig. 8.2a, potentially due to the different porosity observed in the two samples. Nonetheless, the geometry had an influence in the resultant porosity of the samples since the cylinders in fig. 8.1a exhibit grater variance opposed to their geometrical counterparts, as displayed in fig. 8.1b. Overall, it seems that the cylinder shape is more susceptible to the process parameters compared to the conical geometry. This result is most probably related to the different heat extraction capacity of the two geometries, already discussed in section 7.3.1.

8.3 STATISTICAL ANALYSIS

Similar to the previous chapter, herein are summarized the statistical analysis done on the HV measurements taken. Although no particular correlation is found, it is the author's care to give a complete and exhaustive description of the work done. In the following one-way ANOVA analysis both assumptions needed to validate the test have been checked; hence, all

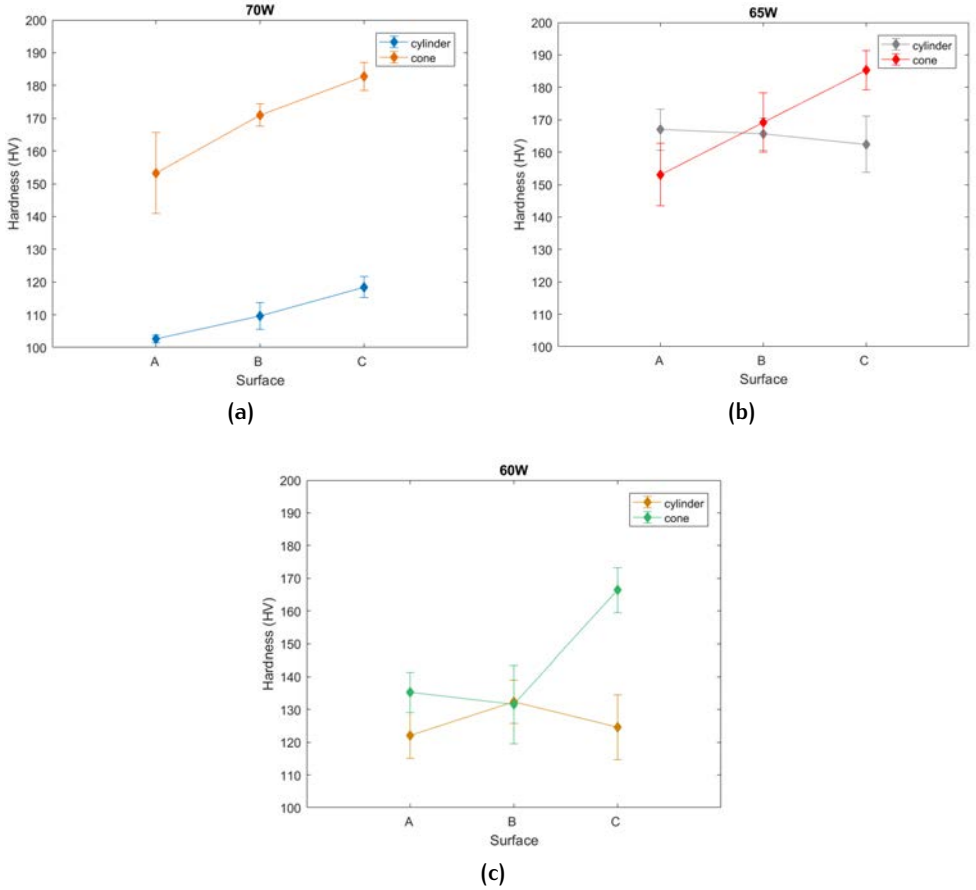

Figure 8.2. Summary of the Vickers hardness tests of: (a) 70 *W* printing series; (b) 65 *W* printing series; (c) 60 *W* printing series.

the data are normally distributed and the variance across groups (i.e. print parts) are homogeneous. Nonetheless, in section 8.3.1 will be displayed the plots for one representative sample.

8.3.1 Heights comparison

In fig. 8.1 most of the samples exhibit an increase in Vickers hardness going from surface A to surface C (i.e. increasing height). Therefore, ANOVA tests have been made to investigate if there is a statistical difference between the data taken at each surface. Although, it has to be kept in mind that the datasets' dimensions are not as big as the melt pools depth measurements used in the analysis in section 7.4. Anyhow, the 70 *W* cylinder has been used to display the following plots in fig. 8.3, representative of the other samples.

As it can be seen, fig. 8.3b do not align with a horizontal line, thus it would seems that the homogeneity assumption needed for the ANOVA is not satisfied. However, when a mathematical approach is used the result lead to the opposite conclusion. In fact, Levene's test for homogeneity of variance return a p-value of 0.333 higher than the significance level of 0.05. Therefore, there is no evidence to suggest that the variance across groups is statistically significantly different; in other words it can be assumed homogeneity of variance among the surfaces. The dataset's boxplot in fig. 8.3c clearly remark the difference between the mean hardness of each surface; moreover the absence of outliers further validate the mean values displayed in the boxplot since they have not been affected by them.

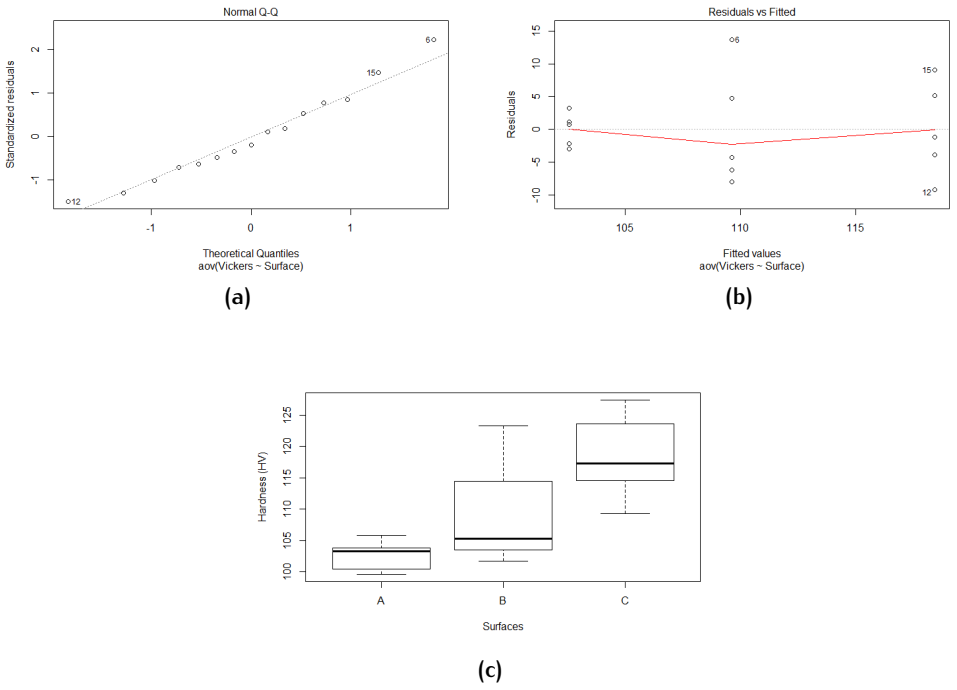

Figure 8.3. Plots representing the data taken from the 70 *W* cylinder, respectively showing: (a) normality plot of the residuals; (b) homogeneity of variances plot; (c) boxplot to visualize the data.

The results of the ANOVA analysis done on the data gathered at different heights for each sample are summarized in table 8.1. The degree of freedom and their residuals, used to calculate the F-value and P-value, were the same for all the samples: Df = 2 and R = 12 respectively. Most of the p-values are above 0.05, hence there is no statistical difference in the hardness changes

between the surfaces of the same sample. It is also interesting to observe that the conical geometry overall returned p-values around the 0.05 mark. This could imply a possible correlation between a particular geometry and the evolution of HV, which also is a indication of the porosity levels.

Table 8.1. Results of the one-way ANOVA analysis for each sample.

Sample	Factor	Sum square	Mean square	F-value	P-value
70 *W* cylinder	Surface	631.1	315.54	6.722	0.011*
	Residuals	563.3	46.94		
70 *W* cone	Surface	2204	1102	3.65	0.0578
	Residuals	3624	302		
65 *W* cylinder	Surface	53.2	26.6	0.115	0.892
	Residuals	2775.3	231.3		
65 *W* cone	Surface	2598	1299.1	3.687	0.0565
	Residuals	4228	352.4		
60 *W* cylinder	Surface	283	141.6	0.443	0.652
	Residuals	3837	319.7		
60 *W* cone	Surface	3673	1836.3	4.816	0.0291*
	Residuals	4576	381.3		

8.3.2 Geometry comparison

In fig. 8.2 (see section 8.2) each series has been plotted to investigate any possible correlation between geometry and Vickers hardness. Similar to section 7.4.2, instead of comparing each surface's hardness with other's samples one, the dataset referred to the whole sample's measurements, thus avoiding to divide the sample by surfaces. The boxplot of fig. 8.4 displays a remarkable difference in the way the data are distributed, precisely the cones exhibit much wider distribution compared to the cylinders. Furthermore, fig. 8.4a present narrow boxplots with mean values extremely different along with the presence of outliers who could have affected the mean's position of the 70 *W* cone's boxplot. While, fig. 8.4b boxplots show almost the same mean value with the presence of a bottom outlier which affect the mean's position in similar fashion in both datasets. Lastly, fig. 8.4c presents no outliers and the mean values differ much less compared to fig. 8.4a.

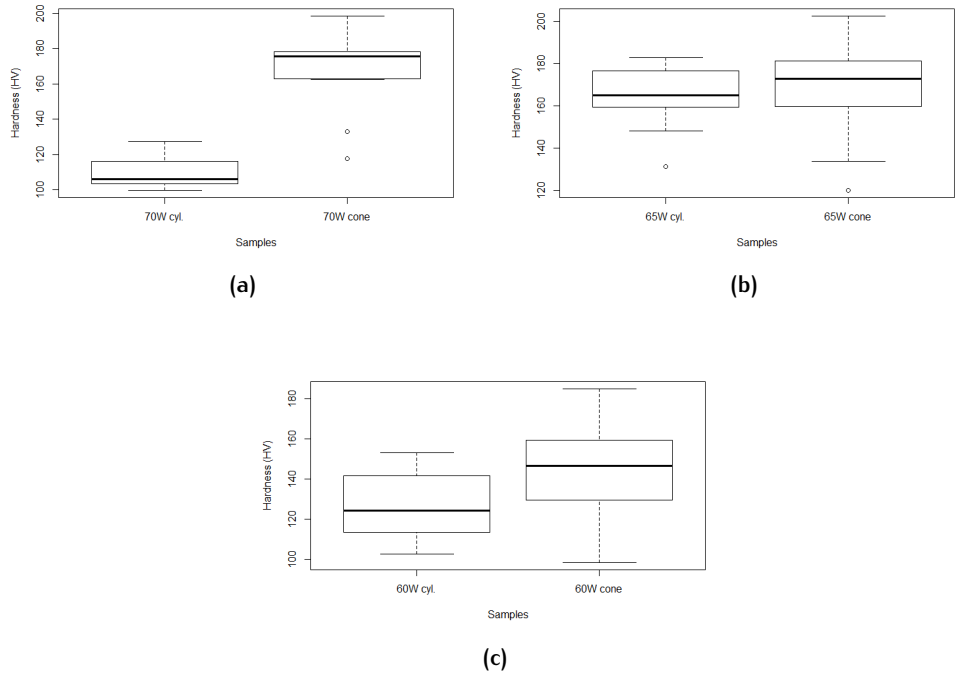

Figure 8.4. Summary of the population of the various samples, respectively: (a) 70 *W* series; (b) 65 *W* series; (c) 60 *W* series.

The ANOVA tests are summarized in table 8.2, the degree of freedom and their residuals were equal in all samples: $\mathtt{Df} = 1$ and $\mathtt{R} = 28$ respectively. By looking at the p-values, it is clear that the observation made above were correct; the 70 *W* and 60 *W* series present a significant difference between the two geometries while the 65 *W* series do not. It is interesting to observe that where the porosity was lower (i.e. 65 *W*) there difference between the geometries is absent. This indicates that the porosity surely affected the HV measurements done, however, it was already taken into account by the author (see section 8.1). Moreover, given the fact that Vickers hardness can also be used as an indicator to evaluate the level of porosity, it won't invalidate the measurement and observation done in this chapter.

Table 8.2. Results of the one-way ANOVA analysis for each series.

Sample	Factor	Sum square	Mean square	F-value	P-value
70 W series	Surface	25907	25907	103.3	$6.71 \cdot 10^{-11}$*
	Residuals	7022	251		
65 W series	Surface	132	131.6	0.382	0.542
	Residuals	9655	344.8		
60 W series	Surface	2421	2421.5	5.482	0.0266*
	Residuals	12368	6.441.7		

9 MODEL IMPROVEMENT

It has been decided to try to find a factor useful to better describe the melt pools depths since a trend has been found (see section 7.2), consistent in all the samples analysed and further confirmed by the statistical analysis. Therefore, the aim of this chapter is to further analyse the melt pools depths data to obtain a factor which will improve the analytical model that, currently, is not addressing the trend found so far. An important note is that instead of the parts division utilized in the previous chapters, the melt pools depths of the samples have been assigned to the average position of each part; thus, from part 1 to 4 respectively at 6mm, 21mm, 39mm, 54mm. This division enables to display both the predicted model curve and the sample's data in the same plot by just referring at the distance from the building plate as will be seen in the following.

9.1 CURVE FIT

The melt pool depth curves have been analysed with Matlab, using the curve fitting tool offered by the software. After several interpolations, the best fitting resulted to be linear as represented in the formula in eq. (9.1), where x represents the distance from the building plate (i.e. the height) quantified in millimetres and f(x) is the predicted depth of the melt pools. The coefficients of the polynomial are summarized in the table 9.1. Two additional values are displayed to give an indication of the fit quality: the sums of the squares errors (SSE) and the R-square.

$$f(x) = p1 \cdot x + p2 \tag{9.1}$$

Table 9.1. Summary of the experimental data curve fit results.

Laser power (*W*)	Sample's shape	p1	p2 (µm)	SSE	R-square
70	Cylinder	-0.16160	34.13	2.265	0.9381
	Cone	-0.11260	31.46	0.1580	0.9928
65	Cylinder	-0.12890	31.11	0.1470	0.9718
	Cone	-0.09370	28.75	0.1813	0.9892
60	Cylinder	-0.06212	26.94	1.4280	0.8898
	Cone	-0.05553	26.31	0.1546	0.9632

A good fit was achieved in almost every sample, as indicated both by the SSE values being close to zero and the R-squares being near the unity. This further confirm the linear correlation between the melt pools depths and the distance from the building plate found during the microstructural characterization. An interesting note is that the slope coefficients tend to decrease with decreasing laser power. This could be explained considering that a lower energy source would result in a more stable printing with lower accumulation of heat inside the print. Furthermore, at constant laser power the cones exhibit lower slopes compared to the cylinders. However, given the non statistical significance found in section 7.4.2 it has been decided to apply the same factor proposition for both the geometries (see section 9.2). Before proceeding, a preliminary analysis was made with the use of the results from the curve fit analysis since the linear correlation seems to be a good fit for the data. Therefore, by using the same formula reported in eq. (9.1) the average slope of the curves has been calculated, resulting in an absolute value of $p1^* = -0.1024$; while the starting depth, i.e. p2, has been taken considering the prediction of the analytical model reported in the table below and already mentioned in chapter 4 (see section 4.3). This approach lead to the same prediction for both geometries and, in that perspective, the plots in fig. 9.1 present the experimental data gathered for each series and the improved model prediction in the same graphs. The distance from the building plate has been considered between the height range of the samples.

In fig. 9.1, the improved model describes the melt pools depth trend, especially in fig. 9.1a; however, an analysis of the residuals has been conducted to quantify the goodness of the factor proposed. The R-square values listed

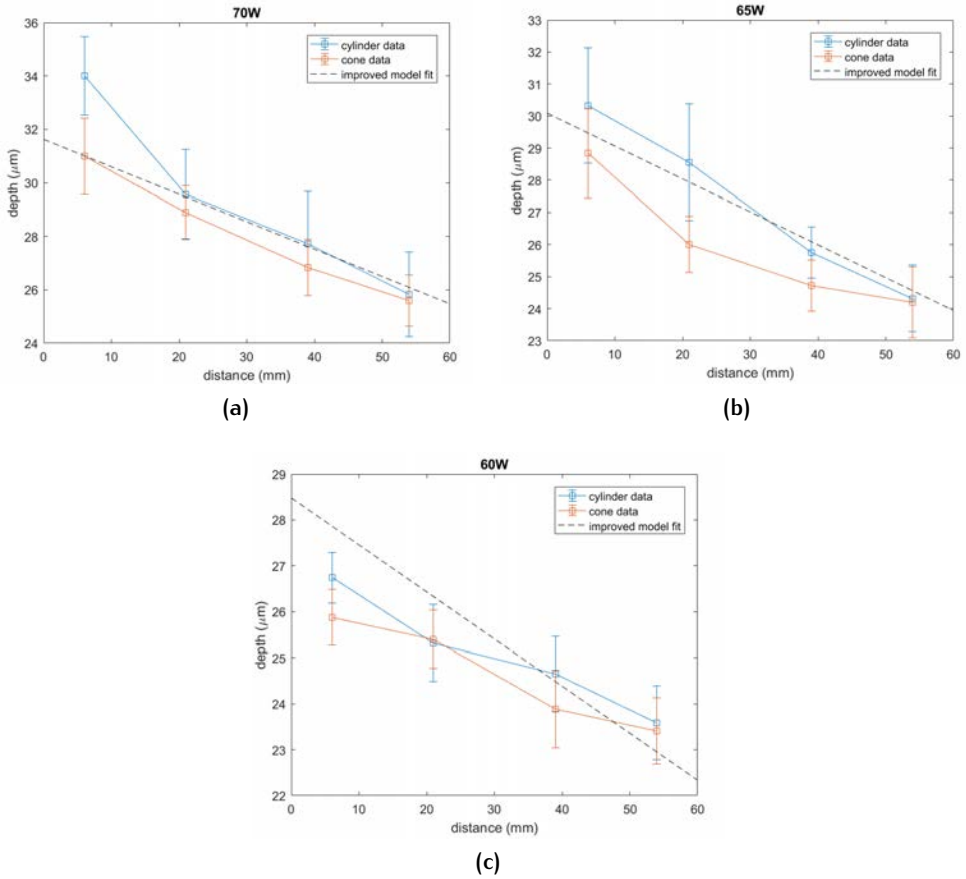

Figure 9.1. Comparison of the improved model trend and the sample's depths data, respectively of: (a) 70 *W* series; (b) 65 *W* series; (c) 60 *W* series.

in table 9.2 show a good fit for certain datasets as the 70 *W* cone and 65 *W* cylinder exhibit; although, the same statement cannot be made for the 60 *W* series. In fact, the model predicted a melt pool depth of 28.48 μm for the 60 *W* series which is affecting the fitting result since the data exhibit lower starting depths values. However, this chapter focus is not on correcting the existing model, instead more attention is given to describe the trend found in the melt pools depths. Therefore, using the slopes average p1 as a rough approximation seems to describe well enough the descending trend. On the other hand, it does not permit an appreciable generalization to other studies and it does not address the influence of laser power on the slopes of the curves as observed in table 9.1.

Table 9.2. Summary of the fit results between the improved model and the experimental data using $p1^*$.

$p1^*$	Laser power (W)	$p2$ (μm)	Sample's shape	SSE	R-square
- 0.1024	70	31.62	Cylinder	3.0083	0.8145
			Cone	1.0874	0.9473
	65	30.09	Cylinder	1.1339	0.9562
			Cone	2.4891	0.6416
	60	28.48	Cylinder	1.6500	0.6087
			Cone	2.3206	0.0397

9.2 FACTOR PROPOSITION

A possible approach to determine a factor able to describe the decrease in melt pools depths while addressing the laser power influence on the curves steepness will be outline in the following section. The form used to describe the trend, given the good fit found in section 9.1, has not been changed and is still a polynomial of the first order as reported in eq. (9.2). While, eq. (9.3) present the linear coefficient g properly defined to take into account the laser power used during the printing, listed as P, X is the height of the envelope and P_{max} refers to the maximum power reachable by the machine. In this project, X and P_{max} are respectively 90 mm and 100 W.

$$f(x) = p2 - g \cdot x \tag{9.2}$$

$$g = \frac{p2}{X} \cdot \left(\frac{P}{P_{max}}\right)^3 \tag{9.3}$$

Similarly to the previous section, the plots representing this new model and the experimental data are listed in fig. 9.2 and their result summarized in table 9.3. While a good fit has been obtained for both 70 W and 65 W series; the 60 W series present negative R-square values, indicating that a horizontal curve would interpolate the data better. However, by looking at fig. 9.2c it is clear that the offset is on the melt pool depth prediction that make the curve starting point at 28.48 μm, instead of few microns lower. Although less marked, the same problem could also be seen in the previous plots of

fig. 9.1c; this is probably due to the different steepness of the curves, higher in the model with a constant average slope p1* compared to the coefficient g in this section.

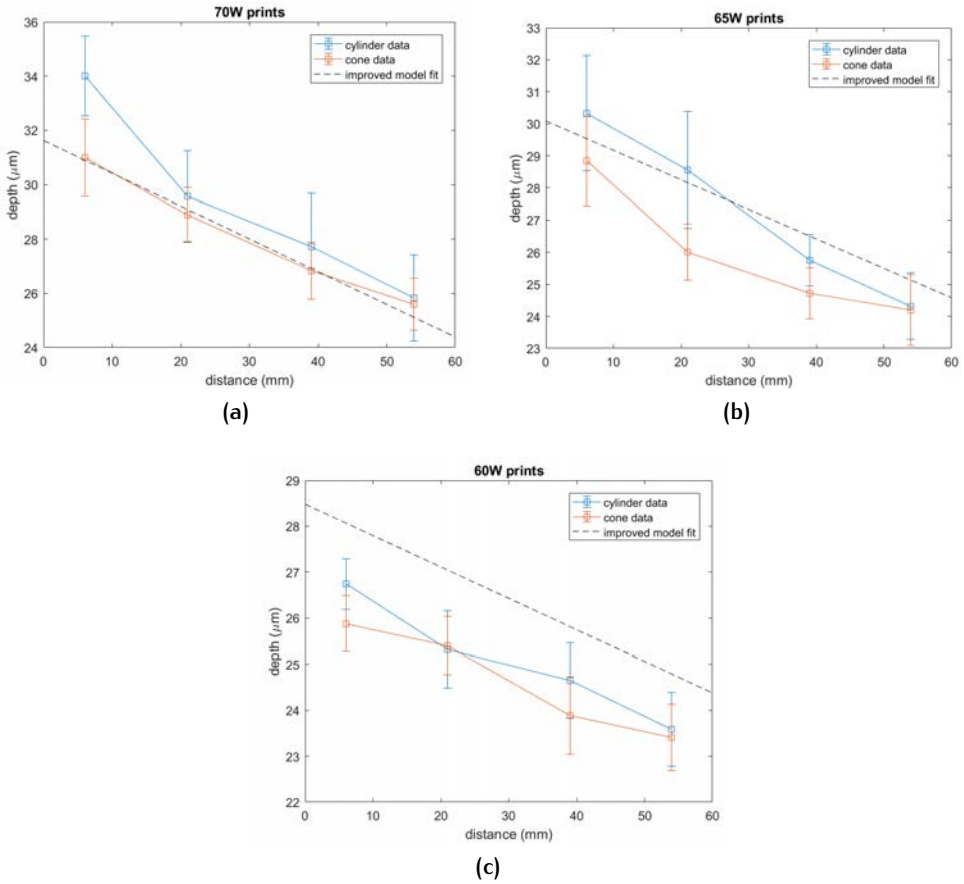

Figure 9.2. Plots of the proposed model and the sample's depths data, respectively of: (a) 70 *W* series; (b) 65 *W* series; (c) 60 *W* series.

Table 9.3. Summary of the fit results between the improved model and the experimental data using p1*.

Laser power (*W*)	Sample's shape	g	p2 (μm)	SSE	R-square
70	Cylinder	0.1205	31.62	3.3234	0.7737
	Cone			0.5371	0.9871
65	Cylinder	0.0918	30.09	1.4158	0.9317
	Cone			3.0415	0.4648
60	Cylinder	0.0684	28.48	2.7452	- 0.0832
	Cone			3.6254	- 1.3439

In fact, the slopes of the curves outlined by the constant g exhibit a good similarity with the values obtained by the curve fit and reported in table 9.1. This observation is further confirmed when the starting melt pool depth of

the 60 *W* series is modified to the average of the experimental data, leading to an adjusted starting value of p2* = 26.63 μm. In this way, the R-square values for the cylinder and cone are 0.9028 and 0.9524 respectively, displaying an almost perfect fit as fig. 9.3present.

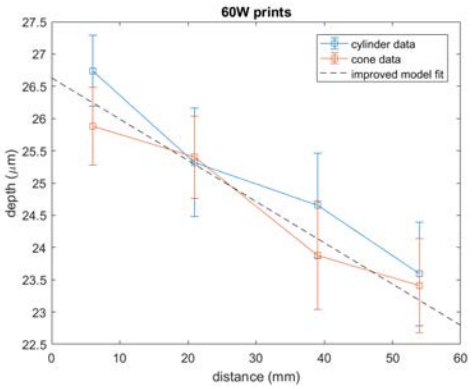

(a)

Figure 9.3. Steepness comparison between the experimental data and the improved model fit.

Part IV

CONCLUSIONS AND FUTURE DEVELOPMENTS

10 CONCLUSIONS

In this work, 316L stainless steel samples made with additive manufacturing powder bed fusion technology, have been characterized; focus has been given to laser power and to part's shape, while their influence over the microstructural evolution and overall sample's quality have been investigated. The influence of geometry on the microstructure, related to the heat extraction capacity, has been addressed by selecting two geometries that displayed different levels of complexity: a cylindrical and conical shape respectively. Among the process parameters, laser power has been selected since it is the main factor influencing the heat source; therefore, it was assumed that its variation would modify the liquid-solid interface velocity and, consequently, the melt pools dimensions. This has been achieved selecting three increasing values of laser power thought to be high enough to enable distinct results.

Microstructural characterizations have been done both on the longitudinal direction, i.e. the whole sample's cross-section, and on three horizontal surfaces at different sample's heights. The microstructural analysis enabled to gain insight about the structure features and to measure the melt pools depths and both widths and lengths, from the cross-sections and the horizontal surfaces respectively. Moreover, Vickers hardness tests have been made on the horizontal surfaces to further characterize the samples. The obtained results and observations are summarized below.

- The correlation between laser power and the melt pools depths has been observed and quantified, proving the correctness of the implemented model.
- In the same sample, the melt pools depths decreased with increasing distance from the building plate. Although the model has not taken it into account, this correlation has been found consistently in all the

printed samples and further confirmed with the aid of inferential statistic.

- A numerical factor was proposed and successfully improved the implemented model to better fit the melt pools depth data found in this work.
- It has been observed that the melt pools widths and lengths tend to decrease in magnitude in the conical samples if compared to their cylindrical counterpart.
- The conical geometry exhibited higher Vickers hardness and it was overall less influenced by the laser power, resulting in better quality of the printed samples in terms of density.

10.1 FUTURE WORKS

As a future development, a quantification of the porosity could be done to better characterize the samples and give more quantitative information about the influence that laser power and geometry had on the printings. Possible future studies could focus on confirming the results obtained in the project and validate the improved model that has been proposed, given the statistical significance found on the melt pools depths dataset. Furthermore, a way to better highlight the melt pools depths evolution could be researched either by changing the samples' height with the same geometry, thus increasing the distance from the building plate, or by increasing the gap in between the laser power levels to better highlight the effect of laser power.

BIBLIOGRAPHY

[1] Eleonora Atzeni and Alessandro Salmi. "Economics of additive manufacturing for end-usable metal parts". In: *The International Journal of Advanced Manufacturing Technology* 62.9-12 (Feb. 2012), pp. 1147–1155.

[2] F. Bartolomeu et al. "316L stainless steel mechanical and tribological behavior—A comparison between selective laser melting, hot pressing and conventional casting". In: *Additive Manufacturing* 16 (Aug. 2017), pp. 81–89.

[3] Barry Berman. "3-D printing: The new industrial revolution". In: *Business Horizons* 55.2 (Mar. 2012), pp. 155–162.

[4] Umberto Scipioni Bertoli, Benjamin E. MacDonald, and Julie M. Schoenung. "Stability of cellular microstructure in laser powder bed fusion of 316L stainless steel". In: *Materials Science and Engineering: A* 739 (Jan. 2019), pp. 109–117.

[5] C. D. Boley, S. A. Khairallah, and A. M. Rubenchik. "Modeling of Powder Absorption in Additive Manufacturing". In: *CLEO: 2014*. OSA, 2014.

[6] Joon-Phil Choi et al. "Evaluation of Powder Layer Density for the Selective Laser Melting (SLM) Process". In: *MATERIALS TRANSACTIONS* 58.2 (2017), pp. 294–297.

[7] Hahn Choo et al. "Effect of laser power on defect, texture, and microstructure of a laser powder bed fusion processed 316L stainless steel". In: *Materials & Design* 164 (Feb. 2019), p. 107534.

[8] Joseph R Davis et al. *Stainless steels*. ASM international, 1994.

[9] Montasser M. DEWIDAR, Khalil A KHALIL, and J.K. LIM. "Processing and mechanical properties of porous 316L stainless steel for biomedical applications". In: *Transactions of Nonferrous Metals Society of China* 17.3 (June 2007), pp. 468–473.

[10] Alexandre Dolgui and Jean-Marie Proth. *Supply Chain Engineering*. Springer London, 2010.

[11] Daniel R. Eyers and Andrew T. Potter. "Industrial Additive Manufacturing: A manufacturing systems perspective". In: *Computers in Industry* 92-93 (Nov. 2017), pp. 208–218.

[12] M.M. Francois et al. "Modeling of additive manufacturing processes for metals: Challenges and opportunities". In: *Current Opinion in Solid State and Materials Science* 21.4 (Aug. 2017), pp. 198–206.

[13] William E. Frazier. "Metal Additive Manufacturing: A Review". In: *Journal of Materials Engineering and Performance* 23.6 (Apr. 2014), pp. 1917–1928.

[14] Ian Gibson, David W. Rosen, and Brent Stucker. "Design for Additive Manufacturing". In: *Additive Manufacturing Technologies*. Springer US, 2010, pp. 299–332.

[15] Ronald M. Gilgenbach. "S.I. Anisimov and V.A. Khokhlov, Instabilities in Laser-Matter Interaction, CRC Press, Boca Raton, FL (1995). 141 pages, 99.95(U.S.)/120.00(Foreign).ISBN0–8493 − 8660–8.". In: *Laser and Particle Beams* 14.04 (Dec. 1996), p. 797.

[16] Larry Greenemeier. "NASA plans for 3-D printing rocket engine parts could boost larger manufacturing trend". In: *Scientific American* (2012).

[17] Hengfeng Gu et al. "Influences of energy density on porosity and microstructure of selective laser melted 17-4PH stainless steel". In: *2013 Solid Freeform Fabrication Symposium*. Vol. 474. 2013.

[18] *Guide for Characterizing Properties of Metal Powders Used for Additive Manufacturing Processes*.

[19] A.V. Gusarov and I. Smurov. "Modeling the interaction of laser radiation with powder bed at selective laser melting". In: *Physics Procedia* 5 (2010), pp. 381–394.

[20] Abid Haleem, Mohd Javaid, and Anil Saxena. "Additive manufacturing applications in cardiology: A review". In: *The Egyptian Heart Journal* 70.4 (Dec. 2018), pp. 433–441.

[21] W.S.W. Harun et al. "A review of powder additive manufacturing processes for metallic biomaterials". In: *Powder Technology* 327 (Mar. 2018), pp. 128–151.

[22] Michael J. Heiden et al. "Evolution of 316L stainless steel feedstock due to laser powder bed fusion process". In: *Additive Manufacturing* 25 (Jan. 2019), pp. 84–103.

[23] E Herderick. "Additive manufacturing of metals: A review". In: *Materials Science and Technology* MS (2011), p. 1413.

[24] Dirk Herzog et al. "Additive manufacturing of metals". In: *Acta Materialia* 117 (Sept. 2016), pp. 371–392.

[25] Samuel H. Huang et al. "Additive manufacturing and its societal impact: a literature review". In: *The International Journal of Advanced Manufacturing Technology* 67.5-8 (Oct. 2012), pp. 1191–1203.

[26] Yong Huang et al. "Additive Manufacturing: Current State, Future Potential, Gaps and Needs, and Recommendations". In: *Journal of Manufacturing Science and Engineering* 137.1 (Nov. 2014), p. 014001.

[27] Alexander Ilin et al. "Computer Aided Optimisation of the Thermal Management During Laser Beam Melting Process". In: *Physics Procedia* 56 (2014), pp. 390–399.

[28] BSEN ISO. *6507-1: 2018—Metallic Materials—Vickers Hardness Test—Part 1: Test Method*. 2018.

[29] Mohd. Javaid and Abid Haleem. "Additive manufacturing applications in medical cases: A literature based review". In: *Alexandria Journal of Medicine* (Oct. 2017).

[30] Mohd. Javaid and Abid Haleem. "Additive manufacturing applications in orthopaedics: A review". In: *Journal of Clinical Orthopaedics and Trauma* 9.3 (July 2018), pp. 202–206.

[31] Chandrika Kamath et al. "Density of additively-manufactured, 316L SS parts using laser powder-bed fusion at powers up to 400 W". In: *The International Journal of Advanced Manufacturing Technology* 74.1-4 (May 2014), pp. 65–78.

[32] Saad A. Khairallah and Andy Anderson. "Mesoscopic simulation model of selective laser melting of stainless steel powder". In: *Journal of Materials Processing Technology* 214.11 (Nov. 2014), pp. 2627–2636.

[33] W. E. King et al. "Laser powder bed fusion additive manufacturing of metals physics, computational, and materials challenges". In: *Applied Physics Reviews* 2.4 (Dec. 2015), p. 041304.

[34] Wayne E. King et al. "Observation of keyhole-mode laser melting in laser powder-bed fusion additive manufacturing". In: *Journal of Materials Processing Technology* 214.12 (Dec. 2014), pp. 2915–2925.

[35] J.-P. Kruth, M.C. Leu, and T. Nakagawa. "Progress in Additive Manufacturing and Rapid Prototyping". In: *CIRP Annals* 47.2 (1998), pp. 525–540.

[36] Andelle Kudzal et al. "Effect of scan pattern on the microstructure and mechanical properties of Powder Bed Fusion additive manufactured 17-4 stainless steel". In: *Materials & Design* 133 (Nov. 2017), pp. 205–215.

[37] Alexander Leicht, Uta Klement, and Eduard Hryha. "Effect of build geometry on the microstructural development of 316L parts produced by additive manufacturing". In: *Materials Characterization* 143 (Sept. 2018), pp. 137–143.

[38] Gideon N. Levy, Ralf Schindel, and J.P. Kruth. "RAPID MANUFACTURING AND RAPID TOOLING WITH LAYER MANUFACTURING (LM) TECHNOLOGIES, STATE OF THE ART AND FUTURE PERSPECTIVES". In: *CIRP Annals* 52.2 (2003), pp. 589–609.

[39] Hod Lipson and Melba Kurman. *Fabricated: The New World of 3D Printing*. 1st. Wiley Publishing, 2013. ISBN: 1118350634, 9781118350638.

[40] Fencheng Liu et al. "The effect of laser scanning path on microstructures and mechanical properties of laser solid formed nickel-base superalloy Inconel 718". In: *Journal of Alloys and Compounds* 509.13 (Mar. 2011), pp. 4505–4509.

[41] James Manyika et al. *Disruptive technologies: Advances that will transform life, business, and the global economy*. Vol. 180. McKinsey Global Institute San Francisco, CA, 2013.

[42] Manyalibo J. Matthews et al. "Denudation of metal powder layers in laser powder bed fusion processes". In: *Acta Materialia* 114 (Aug. 2016), pp. 33–42.

[43] Michael F McGuire. *Stainless steels for design engineers*. Asm International, 2008.

[44] Anne Mertens et al. "Microstructures and Mechanical Properties of Stainless Steel AISI 316L Processed by Selective Laser Melting". In: *Materials Science Forum* 783-786 (May 2014), pp. 898–903.

[45] "Metallography and Microstructures of Stainless Steels and Maraging Steels". In: *Metallography and Microstructures*. ASM International, 2004, pp. 670–700.

[46] Jitka Metelkova et al. "On the influence of laser defocusing in Selective Laser Melting of 316L". In: *Additive Manufacturing* 23 (Oct. 2018), pp. 161–169.

[47] Kenneth C Mills. *Recommended values of thermophysical properties for selected commercial alloys*. Woodhead Publishing, 2002.

[48] Todd M. Mower and Michael J. Long. "Mechanical behavior of additive manufactured, powder-bed laser-fused materials". In: *Materials Science and Engineering: A* 651 (Jan. 2016), pp. 198–213.

[49] Bernhard Mueller. "Additive Manufacturing Technologies – Rapid Prototyping to Direct Digital Manufacturing". In: *Assembly Automation* 32.2 (Apr. 2012).

[50] Vojislav Petrovic et al. "Additive layered manufacturing: sectors of industrial application shown through case studies". In: *International Journal of Production Research* 49.4 (Feb. 2010), pp. 1061–1079.

[51] K. Satish Prakash, T. Nancharaih, and V.V. Subba Rao. "Additive Manufacturing Techniques in Manufacturing -An Overview". In: *Materials Today: Proceedings* 5.2 (2018), pp. 3873–3882.

[52] David W Rosen. "Additive Manufacturing Technologies: Opportunities for Customization, Flexibility, Complexity, and Simplicity". In: *Advanced Technology and the Future of US Manufacturing* (2004), p. 34.

[53] Alexander M. Rubenchik, Wayne E. King, and Sheldon S. Wu. "Scaling laws for the additive manufacturing". In: *Journal of Materials Processing Technology* 257 (July 2018), pp. 234–243.

[54] M Ruffo and R Hague. "Cost estimation for rapid manufacturing ' simultaneous production of mixed components using laser sintering". In: *Proceedings of the Institution of Mechanical Engineers, Part B: Journal of Engineering Manufacture* 221.11 (Nov. 2007), pp. 1585–1591.

[55] K. Saeidi et al. "Hardened austenite steel with columnar sub-grain structure formed by laser melting". In: *Materials Science and Engineering: A* 625 (Feb. 2015), pp. 221–229.

[56] Seshadev Sahoo and Kevin Chou. "Phase-field simulation of microstructure evolution of Ti–6Al–4V in electron beam additive manufacturing process". In: *Additive Manufacturing* 9 (Jan. 2016), pp. 14–24.

[57] W. J. Sames et al. "The metallurgy and processing science of metal additive manufacturing". In: *International Materials Reviews* 61.5 (Mar. 2016), pp. 315–360.

[58] Aude Simar, Stéphane Godet, and Thomas R. Watkins. "Highlights of the special issue on metal additive manufacturing". In: *Materials Characterization* 143 (Sept. 2018), pp. 1–4.

[59] Panagiotis Stavropoulos et al. "Addressing the challenges for the industrial application of additive manufacturing: Towards a hybrid solution". In: *International Journal of Lightweight Materials and Manufacture* 1.3 (Sept. 2018), pp. 157–168.

[60] Ming Tang, P. Chris Pistorius, and Jack L. Beuth. "Prediction of lack-of-fusion porosity for powder bed fusion". In: *Additive Manufacturing* 14 (Mar. 2017), pp. 39–48.

[61] *Terminology for Additive Manufacturing - General Principles - Terminology*.

[62] *Test Method for Knoop and Vickers Hardness of Materials*.

[63] Lore Thijs et al. "A study of the microstructural evolution during selective laser melting of Ti–6Al–4V". In: *Acta Materialia* 58.9 (May 2010), pp. 3303–3312.

[64] Douglas S. Thomas. *Economics of the U.S. Additive Manufacturing Industry*. Tech. rep. Aug. 2013.

[65] Douglas S. Thomas and Stanley W. Gilbert. *Costs and Cost Effectiveness of Additive Manufacturing*. Tech. rep. Dec. 2014.

[66] D. Umbrello, R. M'Saoubi, and J.C. Outeiro. "The influence of Johnson–Cook material constants on finite element simulation of machining of AISI 316L steel". In: *International Journal of Machine Tools and Manufacture* 47.3-4 (Mar. 2007), pp. 462–470.

[67] George F. Vander Voort, ed. *Metallography and Microstructures*. ASM International, 2004.

[68] Di Wang et al. "Investigation of crystal growth mechanism during selective laser melting and mechanical property characterization of 316L stainless steel parts". In: *Materials & Design* 100 (June 2016), pp. 291–299.

[69] Xianglong Wang et al. “Microstructure and mechanical properties of stainless steel 316L vertical struts manufactured by laser powder bed fusion process”. In: *Materials Science and Engineering: A* 736 (Oct. 2018), pp. 27–40.

[70] Lien Chin Wei et al. “Thermal conductivity of metal powders for powder bed additive manufacturing”. In: *Additive Manufacturing* 21 (May 2018), pp. 201–208.

[71] S. W. Williams et al. “Wire Arc Additive Manufacturing”. In: *Materials Science and Technology* 32.7 (Feb. 2016), pp. 641–647.

[72] Kaufui V. Wong and Aldo Hernandez. “A Review of Additive Manufacturing”. In: *ISRN Mechanical Engineering* 2012 (2012), pp. 1–10.

[73] Mostafa Yakout, M.A. Elbestawi, and Stephen C. Veldhuis. “A study of thermal expansion coefficients and microstructure during selective laser melting of Invar 36 and stainless steel 316L”. In: *Additive Manufacturing* 24 (Dec. 2018), pp. 405–418.

[74] E. Yasa and J-P. Kruth. “Microstructural investigation of Selective Laser Melting 316L stainless steel parts exposed to laser re-melting”. In: *Procedia Engineering* 19 (2011), pp. 389–395.

[75] Meng Zhang et al. “Fatigue and fracture behaviour of laser powder bed fusion stainless steel 316L: Influence of processing parameters”. In: *Materials Science and Engineering: A* 703 (Aug. 2017), pp. 251–261.

[76] Yuan Zhong et al. “Intragranular cellular segregation network structure strengthening 316L stainless steel prepared by selective laser melting”. In: *Journal of Nuclear Materials* 470 (Mar. 2016), pp. 170–178.